CHALMERS
UNIVERSITY OF TECHNOLOGY

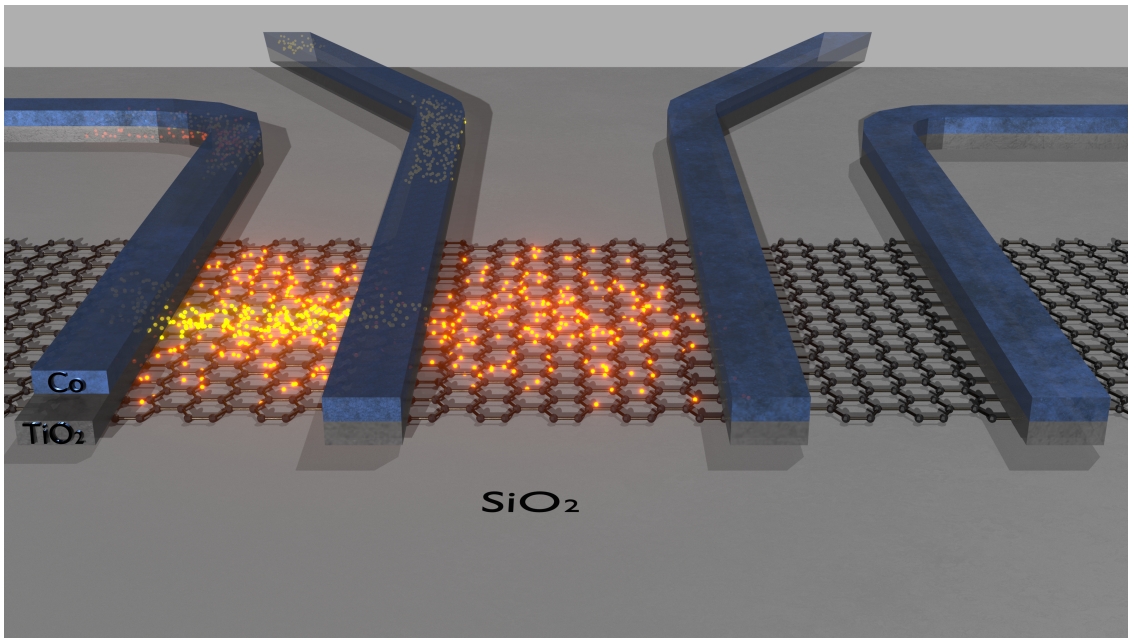

Spin transport in scalable graphene spintronic devices

A study into the geometrical dependence of spin transport parameters in spintronic devices using graphene as transport layer and Co/TiO_2 FM/TB contacts

Master's thesis in Nanotechnology

MARCUS GÖRANSSON

DEPARTMENT OF MICROTECHNOLOGY AND NANOSCIENCE
CHALMERS UNIVERSITY OF TECHNOLOGY
Gothenburg, Sweden 2025
www.chalmers.se

Master's thesis 2025

Spin transport in scalable graphene spintronic devices

A study into the geometrical dependence of spin transport parameters in spintronic devices using graphene as transport layer and Co/TiO_2 FM/TB contacts

MARCUS GÖRANSSON

CHALMERS
UNIVERSITY OF TECHNOLOGY

Department of Microtechnology and Nanoscience
Division of Quantum Device Physics
Spintronics Group
Chalmers University of Technology
Gothenburg, Sweden 2025

Spin transport in scalable graphene spintronic devices
A study into the geometrical dependence of spin transport parameters in spintronic devices using graphene as transport layer and Co/TiO_2 FM/TB contacts
MARCUS GÖRANSSON

Supervisor: Lars Sjöström, Microtechnology and Nanoscience, Chalmers University of Technology
Examiner: Saroj Dash, Microtechnology and Nanoscience, Chalmers University of Technology

Master's Thesis 2025
Department of Microtechnology and Nanoscience
Division of Quantum Device Physics
Spintronics Group
Chalmers University of Technology
SE-412 96 Gothenburg
Telephone +46 31 772 1000

Cover: Non-local four terminal spin valve or Hanle precession measurement setup on a spintronic device with graphene as spin transport layer and Co/TiO_2 ferromagnetic/tunnel barrier contacts. Yellow dots is charge current (I) while orange dots is spin current (I_S).

Typeset in LaTeX
Gothenburg, Sweden 2025

Spin transport in scalable graphene spintronic devices
A study into the geometrical dependence of spin transport parameters in spintronic devices using graphene as transport layer and Co/TiO_2 FM/TB contacts
Marcus Göransson
Department of Microtechnology and Nanoscience
Chalmers University of Technology

Abstract

Spintronics is considered as one of many technologies used to go *Beyond Moore's law* and has special interest within information storage and processing. The performance of spintronic devices are dependent on the spin properties of its spin transport layer and the spin injection and detection efficiency. Ever since the discovery of graphene 2D materials has been of interest for spintronics, where previous research has concluded that graphene has excellent spin transport properties. Spin current can be injected and detected using a magnetic material, where previous research has found using a ferromagnet for this purpose together with a tunnel barrier creates contacts with high spin injection/detection efficiency.

In this thesis, spintronic devices were designed and fabricated using graphene as spin transport layer together with Co/TiO_2 contacts. Current bias, channel length, channel width and contact width were investigated by measuring both non-local (NL) spin valve and NL Hanle precession measurements to extract spin parameters: voltage amplitude (ΔV_{NL}), spin diffusion length (λ_S), spin diffusion constant (D_S) and spin lifetime (τ_s) and then analysing the parameters dependence of investigated factors. On top of this, Hanle spin angle φ were also measured to determine the angle of measured spin current. The project was successful in measuring spin signals for uniform and non-uniform spintronic devices with channel width between $1 - 3$ μm. It was concluded that ΔV_{NL} has a linear current bias dependence while none of the other spin parameters showed any current bias dependence. It was concluded that more measurements are needed to draw any conclusion about channel length, channel width or contact width dependence.

Keywords: Spintronics, Graphene, Beyond Moore's law, 2D materials, Spin valve, Hanle precession, Room temperature

"Learn from yesterday, live for today, hope for tomorrow.
The important thing is not to stop questioning."

– Albert Einstein

Acknowledgements

This master's thesis has given me immense experience and knowledge about nanotechnology, nanofabrication, physics and other matters. I would like to express my gratitude to all those who have supported me and made this project possible.

First and foremost, I want to express my gratitude to my supervisor Professor Saroj Prasad Dash. Your knowledge, guidance, feedback, ideas and encouragement were instrumental in shaping the direction of this project and greatly appreciated.

Second, I want to express my gratitude to my assistant supervisor Lars Sjöström. Thank you for guiding me with fabrication, measurements and analysis as well as giving great feedback and encouragement. This project would have taken a lot longer if not for your guidance.

Third, I want to express my gratitude to my fellow thesis students under quantum device physics group with whom I had fruitful discussions and great laughs. Thank you for making the project more enjoyable.

The fabrication part of this project was performed in Myfab Chalmers, and I want to express my gratitude to the staff there for letting me use their tools to fabricate devices.

Lastly, I want to express my gratitude to my friends and family for their support, encouragement and love throughout this journey. I could not have done this without you, so thank you!

Marcus Göransson, Gothenburg, May 2025

List of Acronyms

Below is the list of acronyms that have been used throughout this thesis listed in alphabetical order:

2D	Two-Dimensional
2T	Two Terminal
4T	Four Terminal
AES	Auger Electron Spectroscopy
AP	Anti Parallel
BAP	Bir-Arnov-Pikus
BLG	Bi-Layer Graphene
CVD	Chemical Vapor Deposition
DOS	Density Of States
DP	D'yakonov-Perel'
EBL	Electron Beam Lithography
EB-PVD	Electrom-Beam Physical Vapor Deposition
EY	Elliot-Yafet
FM	FerroMagnetic
HF	HyperFine
IPA	IsoPropanyl Alcohol
NL	Non-Local
NM	Non-Magnetic
P	Parallel
RT	Room Temperature
SEM	Scanning Electron Microscopy
SLG	Single-Layer Graphene
SNR	Signal-to-Noise Ratio
SOC	Spin-Orbit Coupling
SPR	Surface Plasmon Resonance
TB	Tunnel Barrier

Nomenclature

Below is the nomenclature of indices, parameters and variables that have been used throughout this thesis.

Indices

$\uparrow$,$\downarrow$	Indices for spin up and spin down states
s	Index for spin parameter
NM	Index for non-magnetic parameter
FM	Index for ferro-magnetic parameter
TB	Index for tunnel barrier parameter
NL	Index for non-local parameter
$\parallel$,$\perp$	Indices for parallel and perpendicular
x, y, z	Indices for coordinate direction

Parameters

e	Elementary charge
c	Speed of light
g	Landé g-factor
$\hbar$	Reduced Planck's constant
t	Time
x	Distance
L	Channel length
A	Cross section
W	Width
W_{Gr}	Graphene width
$N_{\uparrow\downarrow}$	Number of available spin up or spin down states

P	Spin polarisation
β	Intrinsic spin polarisation
σ	Conductivity
$\sigma_{\uparrow\downarrow}$	Spin dependent conductivity
σ_{FM}	Conductivity for ferromagnetic material
σ_{NM}	Conductivity for non-magnetic material
D_c	Charge diffusion constant
$D_{\uparrow\downarrow}$	Spin dependent diffusion constant
$v_{F\uparrow\downarrow}$	Spin dependent Fermi velocity
$\vec{v}$	Velocity
$l_{e\uparrow\downarrow}$	Spin dependent mean path of the electron
μ	Chemical potential
$\mu_{\uparrow\downarrow}$	Spin dependent chemical potential
μ_0	Chemical potential splitting at $x = 0$
μ_B	Bohr magneton
λ_s	Spin diffusion length
λ_{FM}	Penetration depth for ferromagnetic material
λ_{NM}	Penetration depth for non-magnetic material
$j_{\uparrow\downarrow}$	Spin dependent current density
τ_s	Average spin lifetime
$\tau_{\uparrow\downarrow}$	Average time to flip from spin up to spin down
$\tau_{\downarrow\uparrow}$	Average time to flip from spin down to spin up
I	Current
$I_{\uparrow\downarrow}$	Spin dependent current
I_c	Charge current
I_s	Spin current
γ	Spin polarisation of current
γ_i	Spin polarisation at injectors interface
γ_d	Spin polarisation at detectors interface
R	Resistance
$R^{TB}_{\uparrow\downarrow}$	Spin dependent resistance in tunnel barrier
R_{NM}	Resistance in non-magnetic material
$R_\square$	Square resistance
$E_{k\uparrow}$	Spin up energy level at momentum wave number k

$E_{k\downarrow}$	Spin down energy level at momentum wave number k
$\vec{E}$	Electrical field
$B_{\perp}$	Perpendicular magnetic field
$B_{\parallel}$	Parallel magnetic field
$\vec{B}$	Magnetic field
V_{NL}	Non-local voltage
V_{inj}	Voltage from injected current
$V_{NL,Avg}$	Average non-local voltage signal
$V_{NL,P}$	Non-local voltage signal for parallel magnetisation
$V_{NL,AP}$	Non-local voltage signal for anti parallel magnetisation
$V_{NL}^{\parallel}$	Symmetric component of Hanle signal
$V_{NL}^{\perp}$	Asymmetric component of Hanle signal
ω_L	Spin precession with the Larmor frequency
φ	Angle between injected and detected spin polarization

Variables

$P(x,t)$	Probability of a diffusing spin to preserve its spin state at distance x from the injector ($x = 0$) after time t
$\mu(x, B_{\perp})$	Chemical potential at distance x from the injector ($x = 0$) with applied perpendicular magnetic field $B_{\perp}$
$V_{NL}(L, B_{\perp})$	Non-local voltage at distance L from injector with applied perpendicular magnetic field $B_{\perp}$

Contents

List of Figures

1
Introduction

Ever since Shockley, Bardeen and Brattain invented the transistor in 1947 [1], the transistor has been the core of modern computer science and the core component for logic gates. The transistor revolutionized logic gates and modern day electronics, becoming the foundation for digital computing. There has been rapid developments to create microprocessors with more computational power by increasing the number of transistors. This has been done by decreasing the size of each transistors and has followed a prediction from Gordon Moore known as Moore's law, which states that the number of transistors on a microprocessor will double every two years, as shown in Figure 1.1 [2].

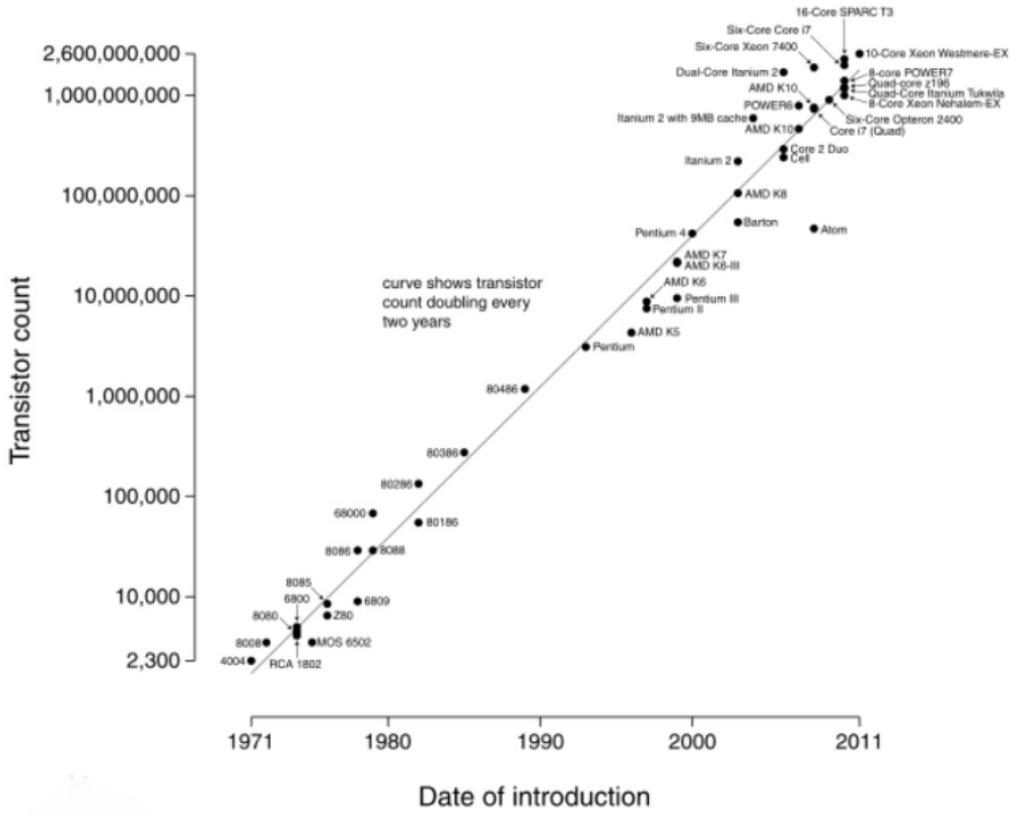

Figure 1.1: Total count of transistors on a microprocessor produced between 1971-2011. The line is Gordon Moore's prediction known as Moore's law. Adapted from [2].

For this to be possible, the size of a transistor must also shrink every two years.

However, this shrinking has slowed down during the recent years as shrinking the size has introduced new problems such as quantum tunnelling and current leakage, creating a physical bottleneck. Due to this, many scholars consider Moore's law to have ended [3] and thus in order to improve our computational power we must go 'beyond Moore's law'.

One of the ways to go 'beyond Moore's law' is to store and process information by manipulating the spin degree of freedom for electrons in solid-state systems. This is knowns as spin electronics, or spintronics [4, 5]. This technology is expected to increase device performance while also decreasing power consumption. However, to realise this one needs to develop spintronic devices with efficient spin injection/detection and long spin diffusion length [9]. This is done by injecting or detecting spin current using magnetic material and by transporting the spin current between injector and detector in a non-magnetic material.

In 2004, Geim and Novoselov proved that 2D materials are possible with the discovery of graphene [6] and in 2010, Geim and Novoselov were awarded the Nobel Prize in Physics for this discovery [7]. Since then, 2D materials have become one of the most active research topics within solid-state physics [8]. Within spintronics, graphene has been particularly interesting as a spin transport material due to its excellent properties such as low spin-orbit coupling and lack of hyperfine interaction causing long spin lifetime in room temperature, high electron mobility and ability to easily be interfaced with materials such as ferromagnets, semiconductors, oxides [9, 10].

However, there are still much to do before this technology can be used for applications. One of spintronics biggest problem is the decay of a spin state which limits the distance information can be carried. A solution to this is to decrease the distance spin has to travel by creating smaller devices, for this reason this thesis will conduct research to investigate the channel length, channel width and contact width dependence for spintronic devices.

2
Theoretical background

To investigate the channel length, channel width and contact width dependence for spintronic devices one has to first understand the theoretical concepts behind spintronics. Here I will present the most important theoretical concepts to understand spintronics and the spin transport layer material: graphene.

2.1 Spin polarisation

Spintronics is fundamentally based on the spin degree of freedom of electrons and is hence important to understand how spin behaves and how it can be manipulated. To understand this, one must understand concepts such as spin lifetime, spin dynamics, spin-orbit interactions, spin transport, spin injection and spin detection. It is common to use a non-magnetic (NM) material for spin transport and a ferromagnetic (FM) material for spin injection/detection since NMs typically have more efficient spin transport properties than FMs, as will be the case for this master's thesis. It is therefore of interest to define spin polarisation of a FM, which comes from its magnetism, that in turn originates from the electron states in the atoms orbitals. When electrons populate the available energy states, they do so by following Pauli exclusion principle and Hund's rules in order to populate the lowest energy states. As Hund's rule states, electrons tend to first populate empty states before pairing opposite spins to fill one state. These unpaired states will have a very small magnetic moment, but for a FM there will be many unpaired states and their combined magnetic moment will create a splitting in the density of states (DOS) at the Fermi level. This means that there will be more available states of one spin (*e.g.* spin-up $N_\uparrow$) and less of the opposite (spin-down $N_\downarrow$) [11]. One can then define the intrinsic spin polarisation of FM as

$$P = \frac{N_\uparrow - N_\downarrow}{N_\uparrow + N_\downarrow}. \tag{2.1}$$

Mott in 1936 [12] found that this spin polarisation P affected the electric conductivity of materials, and explained it by describing the total conductivity of a system σ as the sum of a spin-up $\sigma_\uparrow$ and spin-down $\sigma_\downarrow$ conductivity, *i.e.*

$$\sigma = \sigma_\uparrow + \sigma_\downarrow. \tag{2.2}$$

The spin dependent conductivity can be expressed in the Einstein equation as

$$\sigma_{\uparrow\downarrow} = N_{\uparrow\downarrow} e^2 D_{\uparrow\downarrow}, \text{ where } D_{\uparrow\downarrow} = \frac{1}{3} v_{F\uparrow\downarrow} l_{e\uparrow\downarrow}. \tag{2.3}$$

Here, e is the elementary charge and $D_{\uparrow\downarrow}$ is the spin dependent diffusion constant as a function of the average spin dependent Fermi velocity $v_{F\uparrow\downarrow}$ and the average spin dependent mean path of the electron $l_{e\uparrow\downarrow}$ [13]. The average diffusion constant for a FM can be expressed as

$$\bar{D} = \frac{D_\uparrow D_\downarrow (N_\uparrow + N_\downarrow)}{D_\uparrow N_\uparrow + D_\downarrow N_\downarrow} \tag{2.4}$$

[14] and $\bar{D} = D_c$ for NM, where D_c is the charge diffusion constant [15]. The spin dependent conductivity can then be related to the bulk spin current polarisation P by

$$P = \frac{\sigma_\uparrow - \sigma_\downarrow}{\sigma_\uparrow + \sigma_\downarrow} \tag{2.5}$$

and describes the spin-dependent conductivity for all magnetic metals, semiconductors, insulators and their interfaces with each other or NM materials [11]. This master's thesis will use Cobalt as a FM, which has experimentally obtained a P of 42% [16].

2.2 Spin injection and detection

NM materials have an equilibrium of spin-up ($N_\uparrow$) and spin-down ($N_\downarrow$) states and will therefore have the same conductivity for both spin states. This means that for a FM/NM junction typically used for spin injection, the spin dependant conductivity will be discontinuous. When applying a current through this junction, spins will accumulate at the interface and a splitting of chemical potential μ for opposite states, *i.e.* you have $\mu_\uparrow$ and $\mu_\downarrow$ for spin-up and spin-down. The accumulation of spin at the junction will decay exponentially in the FM and the NM according to their penetration depth λ_{FM} and λ_{NM}, see Figure 2.1 (b). The spin dependent current density $j_{\uparrow\downarrow}$ depends on the spin dependent chemical potential $\mu_{\uparrow\downarrow}$ and the spin dependent conductivity $\sigma_{\uparrow\downarrow}$, it can be expressed as

$$j_{\uparrow\downarrow} = \frac{\sigma_{\uparrow\downarrow}}{e} \partial_x \mu_{\uparrow\downarrow}. \tag{2.6}$$

However, this does not factor in spin flip processes. To include this, one must introduce the spin flip times, which describes average time it takes for a spin-up to flip to spin-down ($\tau_{\uparrow\downarrow}$) and the average time it takes for a spin-down to flip to spin-up ($\tau_{\downarrow\uparrow}$). One can then define the spin lifetime as $\tau_s = (\tau_{\uparrow\downarrow}^{-1} + \tau_{\downarrow\uparrow}^{-1})^{-1}$ and average spin diffusion constant as $D_S = \frac{D_\uparrow D_\downarrow (N_\uparrow + N_\downarrow)}{N_\uparrow D_\uparrow + N_\downarrow D_\downarrow}$. By combining Equation (2.3) and assuming thermal equilibrium (no net scattering: $\frac{N_\uparrow}{\tau_{\uparrow\downarrow}} = \frac{N_\downarrow}{\tau_{\downarrow\uparrow}}$), you can describe the complete spin flip process as

$$\partial_x^2 (\mu_\uparrow - \mu_\downarrow) = \frac{\mu_\uparrow - \mu_\downarrow}{D_s \tau_s}. \tag{2.7}$$

A general solution to this equation is

$$\mu_\uparrow - \mu_\downarrow = \tilde{a} \cdot \exp(-\frac{x}{\lambda_s}) + \tilde{b} \cdot \exp(\frac{x}{\lambda_s}), \tag{2.8}$$

where $\lambda_S = \sqrt{D_s \tau_s}$ is the spin diffusion length, and $\tilde{a}$ and $\tilde{b}$ are integration constants. If charge current is assumed to be conserved and using Equation (2.6), one can derive the chemical potential for both spins as

$$\mu_{\uparrow\downarrow} = a + b \cdot x \pm \frac{c}{\sigma_{\uparrow\downarrow}} \exp(-\frac{x}{\lambda_s}) \pm \frac{d}{\sigma_{\uparrow\downarrow}} \exp(\frac{x}{\lambda_s}). \tag{2.9}$$

By assuming that the spin dependent chemical potential is continuous and the spin current is conserved at the interface along with neglecting interface scattering and resistances, one can define a equilibrium chemical potential as

$$\mu = P\mu_{\uparrow} + (1 - P)\mu_{\downarrow}. \tag{2.10}$$

Using this and defining β as the intrinsic spin polarisation defined in Equation (2.1), a potential difference can be derived as

$$\Delta\mu = \mu_{FM} - \mu_{NM} = \frac{\beta^2(\frac{\lambda_{NM}}{\sigma_{NM}})(\frac{\lambda_{FM}}{\sigma_{NM}}) \cdot eI}{(\frac{\lambda_{FM}}{\sigma_{NM}}) + (1 - \beta^2)(\frac{\lambda_{NM}}{\sigma_{NM}})} \tag{2.11}$$

and the spin polarisation of the current through the interface

$$\gamma = \frac{I_{\uparrow} - I_{\downarrow}}{I_{\uparrow} + I_{\downarrow}} = \frac{\beta \frac{\lambda_{FM}}{\sigma_{FM}}}{\frac{\lambda_{FM}}{\sigma_{FM}} + (1 + \beta^2)\frac{\lambda_{NM}}{\sigma_{NM}}}. \tag{2.12}$$

The main takeaway from these equations are that the spin polarisation depends on the ratios $\frac{\lambda_{FM}}{\sigma_{NM}}$ and $\frac{\lambda_{NM}}{\sigma_{NM}}$. FM has a much smaller spin diffusion length than NM ($\lambda_{FM} \ll \lambda_{NM}$) and the spin polarisation will therefore be lower in FM compared to NM and spins will decay faster. This is a problem, especially since spins injected into the NM tend to diffuse back into the FM due to conductivity mismatch [13].

To mitigate this conductivity mismatch, we will introduce a tunnel barrier (TB) between the FM and NM [17]. TB has a high spin dependent resistance compared to FM and NM (see Figure 2.1 (a) compared to Figure 2.1 (b)) [13]. The TB acts as a 'load' resistance and will not affect the spin polarisation of the current source, hence one can see the spin injection process for FM/TB/NM as an 'ideal' spin current source. Once the spin current is injected, the high spin dependent resistance of the TB decreases the probability of the current to lose its spin information by diffusing back into the FM so much that this problem can be neglected. This will ensure that measurement probes with a TB will have minimal spin relaxation effect on the spin current conducting through the device, increasing the spin relaxation length of the device [14]. For this master's thesis, TiO_2 is used as TB between FM (Co) and NM (graphene).

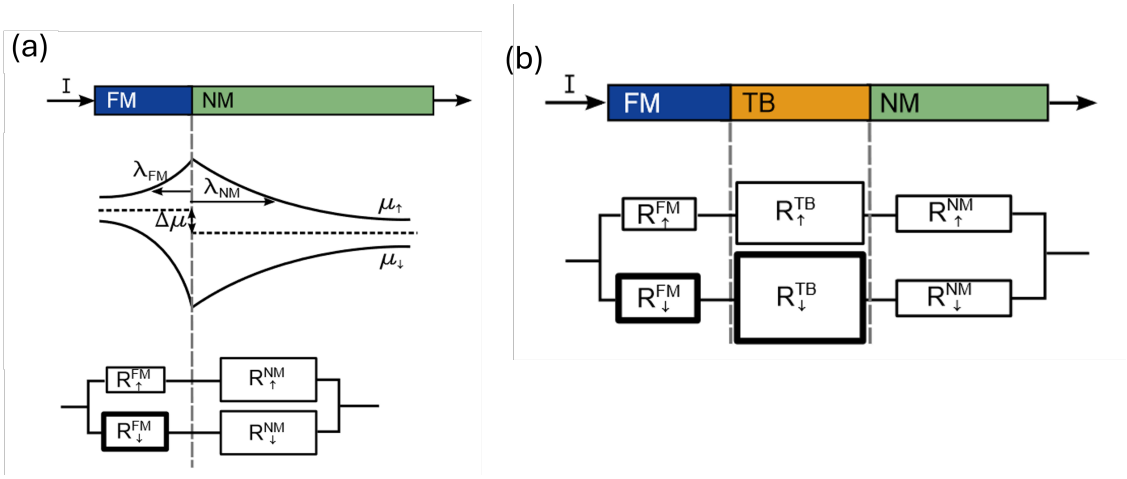

Figure 2.1: Spin current injection through FM/NM and FM/TB/NM interfaces. (a) Schematic of a FM/NM junction where current flows from FM to NM. (b) Spin dependent chemical potentials $\mu_{\uparrow\downarrow}$ at the interface of FM/NM and the penetration depth λ_{FM} for FM and λ_{NM} for NM. There is a chemical potential difference $\Delta\mu$ due to the spin dependent conductivity in FM. (c) Schematic of an equivalent spin dependent resistance network for this FM/NM junction. Note that the spin dependent resistance is higher in NM compared to FM. (d) Schematic of a FM/TB/NM junction where current flows from FM to NM through TB. (e) Schematic of an equivalent spin dependent resistance network for this FM/TB/NM junction. Note that the spin dependent resistance for TB is much higher than both FM and NM. Adapted from [13].

2.2.1 Magnetic domain in FM contact

The spin state injected or detected is dependent on the magnetic domain direction in the FM contact [18]. It is therefore crucial to be able to control the magnetic domain in each contact individually. This is done by applying an external magnetic field to help align the magnetic domains. The strength of the magnetic field required to 'flip' a FM magnetic domain is known as the coercive field and depends on the geometry of FM contact. For rectangular contacts, the magnetic domains tend to align to the easy axis direction (along the long-side) and would need to rotate out of this easy axis direction to 'flip'. The required magnetic field depends on the width of the rectangular contacts, as a wider contact will require a smaller magnetic field than a more narrow contact [19]. A circular contact would not exhibit an easy axis direction due to its uniform geometry, and therefore would change its direction of magnetic domain as soon as an external magnetic field is applied [20].

2.3 Spin decay

Spintronic devices rely on the time and distance a charge carrier can hold a spin state before reaching spin equilibrium. If a medium can stay in a nonequilibrium state long enough, then it allows spin-encoded information to travel far enough to make spintronics a viable technology. Spin relaxation and spin dephasing are two

processes that lead to spin equilibrium and are therefore important to consider when designing spintronic devices and will therefore be introduced in this section [18].

2.3.1 Spin relaxation and spin dephasing

The spin lifetime τ_s and spin diffusion constant D_S define the spin relaxation length (distance charge carrier can travel before losing its spin state):

$$\lambda_s = \sqrt{D_s \tau_s} \tag{2.13}$$

and are therefore two important parameters for spintronics [13]. Spin relaxation and spin dephasing are limited due to spin scattering mechanisms: Elliot-Yafet (EY), D'yakonov-Perel' (DP), Bir-Aronov-Pikus (BAP), hyperfine (HF) interactions and resonant scattering [18], [11]. However, BAP is only relevant for p-doped semiconductors at low temperature [18] and is therefore out of scope for this master's thesis.

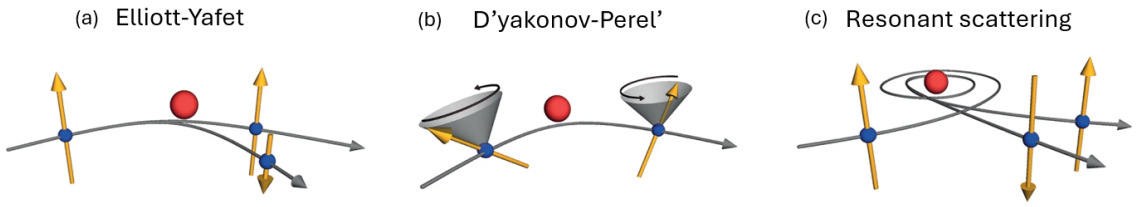

Figure 2.2: Spin scattering mechanisms in graphene. (a) Elliot-Yafet (EY) spin-flip scattering where the red dot is a scattering centre (*e.g.* phonon or impurities), the blue dots are charge carriers with its spin shown as a yellow arrow. (b) D'yakonov-Perel' (DP) can flip a spins state by inversion asymmetry. The red dot represents a scattering centre, the blue dot a charge carrier along with its spin state as a yellow arrow and the grey cone shows the spin precession. (c) Resonant scattering where spin relaxation occurs if a charge carrier has spent enough time around a scattering centre. The red dot is a scattering centre and the blue dot a charge carrier along with its spin state shown as a yellow arrow. Adapted from [21].

2.3.1.1 Elliot-Yafet mechanism

Elliot, in 1954 [22] showed that a lattice that induces spin-orbit coupling (SOC) will also lead to spin relaxation when charge carriers are combined with momentum scattering. Momentum scattering tend to be caused by phonons for high temperature and impurities for low temperatures [18], [22]. Yafet later showed that phonons can also modify the lattice induced SOC leading to further spin relaxation [23]. The EY mechanism is a spin-flip scattering mechanism since the spin relaxation is due to a probability to flip a charge carriers spin state when exposed to the lattice induced SOC and momentum scattering. Because of this, the probability of flipping a spin state will scale with the probability of momentum scattering occurring, which in turn can be increased by *e.g.* increase of atomic mass or increased size of atoms. This means that materials with a low atomic mass (such as graphene) has a low

probability to flip its spin state due to EY mechanism which, in turn increases spin lifetime τ_s [13].

2.3.1.2 D'yakonov-Perel' mechanism

A material can experience inversion asymmetry either by having two distinct atoms present in Bravais lattice (bulk inversion asymmetry, or *Rashba-Dresselhaussen*) or by a built-in or external electric field (structural inversion asymmetry, or *Bychkov-Rashba*) [13]. Inversion asymmetry means that the spin-up and spin-down charge carriers degenerate ($E_{k\uparrow} \neq E_{k\downarrow}$). Bulk inversion asymmetry is common in semiconductors from group III-V (*e.g.* GaAs) and II-VI (*e.g.* ZnSe) as this will introduce two distinct atoms in Bravais lattice [18]. However, bulk inversion asymmetry will not affect pure graphene as it is made of carbon atoms only (group IV) [24]. However, DP spin relaxation will still affect graphene due to structural inversion asymmetry [25]. D'yakonov and Perel' found that this inversion asymmetry was an efficient mechanism of spin relaxation as it results in a electrical field $\vec{E}$ which will induce an effective magnetic field $\vec{B} = \frac{\vec{v}}{c} \times \vec{E}$ that affects spins moving through $\vec{E}$ with velocity $\vec{v}$ (relative to speed of light c), creating a SOC effect [18], [13].

2.3.1.3 Hyperfine interaction

HF interaction is a coupling of the magnetic moments between the electron and the nuclei, if the magnetic moment of the nuclei is non-zero. The magnetic moment of a nuclei is zero if its shells are full, which is the case for graphene. It is worth to note that HF interaction can be introduced to graphene by adding an isotope (*e.g.* ^{13}C) [13], however growing graphene of pure isotope (^{12}C) will not introduce hyperfine interaction effect [26].

2.3.1.4 Resonant scattering

It was first theorised by Duplock *et al.* [27] that magnetic impurities (vacancies or adatoms) can cause resonant spin-flip scattering events, and later experimentally proven by McCreary *et al.* [28]. The impurities create exchange fields, inducing spin relaxation by precession if a charge carrier has spent long enough time in these fields at resonant energies [11].

2.4 Graphene

Graphene is a single layer of graphite, a two-dimensional (2D) ortohexagonal lattice structure of sp^2 hybridised carbon atoms, see Figure 2.3 (a). This ortohexagonal geometry, also referred to as honeycomb geometry has a distance of 0.142 nm between carbon atoms and a thickness of 0.35 nm. Alongside this, graphene has also shown exceptional electrical, magnetic, mechanical and optical properties [29]. It has a Young modulus greater than any other material [30], a intrinsic mobility 100 times higher than Si [31], a current density 6 orders higher than Cu [32], negligible

HF interaction, gate tunability, low spin-orbit coupling and the longest measured spin-relaxation length at room temperature [8]. The single atomic layer also allows graphene to be affected by surrounding material by proximity effect [33]. These properties are essential for transmission and manipulation of spin signals in spintronic devices [8].

The number of layers of graphene affects these exceptional properties [34]. It is therefore important to ensure you have the intended amount of layers when creating a device. This can be investigated using a multitude of methods such as Raman spectroscopy (see Figure 2.3 (f)) [35], Auger electron spectroscopy (AES) [36], scanning electron microscopy (SEM) [37], nano-indention [38], surface plasmon resonance (SPR) [39] and optical reflection microscopy [40]. Even a trained naked eye can detect number of layers [41] due to graphene's optical properties of linear relation between number of layers and graphene light absorption. A single layer of graphene has a light absorption of 2.3%, two layers has 4.6% light absorption [29], see Figure 2.3 (e). For this master's thesis project, monolayer graphene is used.

The honeycomb structure of graphene creates sigma bonds between carbons sp^2 orbitals and π bonds between p_z orbitals, as depicted in Figure 2.3 (c). It is the π bonds which gives graphene the excellent electrical properties as it allows electrons to move freely across the graphene layer. The first Brillouin zone of graphene has six highly symmetrical K points, where both conduction and valence band intersect. These points of interest are known as Dirac points and electrons can freely move between bands which gives graphene its high conductivity, considered the best among known materials at room temperature. The Dirac point is also why graphene is classified as a zero-band-gap semiconductor [29], [42].

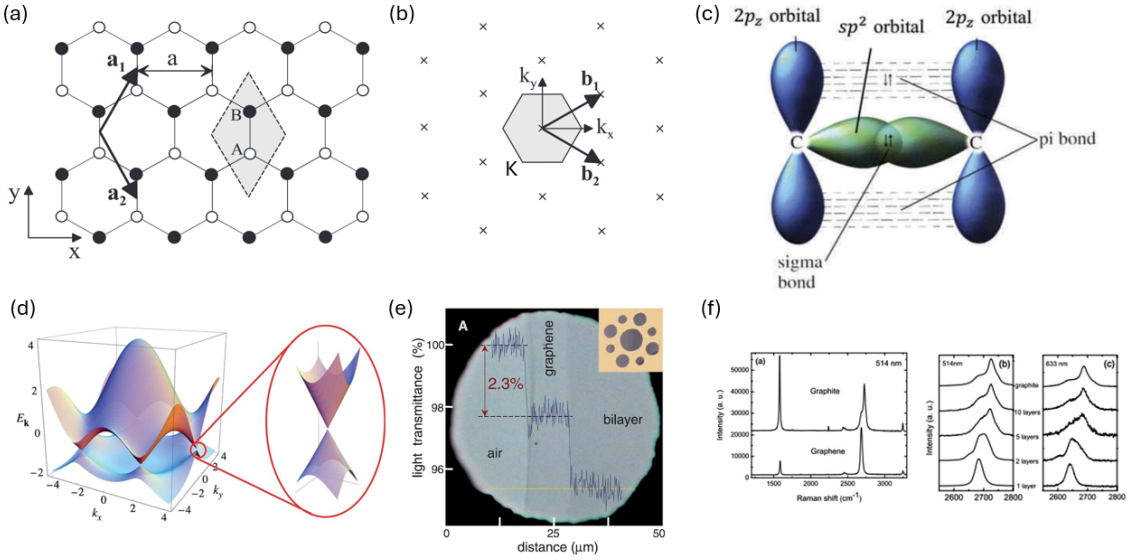

Figure 2.3: Graphene structure and optical properties. (a) Lattice structure of monolayer graphene where white (black) circles show carbon atoms on A (B) sites, creating a hexagonal/honeycomb structure. Vectors $\mathbf{a_1}$ and $\mathbf{a_2}$ are primitive vectors that builds up a unit cell (shaded area). The distance between unit cells is the lattice constant $\mathbf{a}$. Adapted from [34]. (b) The reciprocal lattice of monolayer graphene where crosses shows reciprocal lattice points. Vector $\mathbf{b_1}$ and $\mathbf{b_2}$ are primitive lattice vectors. Shaded area is the first Brillouin zone with six highly symmetrical K points. Adapted from [42]. (c) The sigma and π bonds between each carbon atom in graphene lattice structure. The sigma bond is created between each carbons sp^2 hybridised orbitals and the π bond is created between each carbons p_z orbitals. Adapted from [34]. (d) Band structure of graphene around the first Brillouin zone in reciprocal space. Enhanced inset shows one of 6 symmetrical K points where the Dirac point lies (conduction band and valence band intersect). Adapted from [29]. (e) Optical properties of monolayer and bilayer graphene, where monolayer graphene has a 2.3% light absorption and bilayer graphene a 4.6% light absorption compared to air. Adapted from [29]. (f) Raman spectra of monolayer graphene, graphite and different amount of layers of graphene under different wavelengths. The G peak can be found around 1580 cm^{-1} and the D peak between 1270-1450 cm^{-1}. Adapted from [29].

2.4.1 Spin injection and detection in graphene

Even though graphene has a zero-band-gap structure, its intrinsic resistance is still larger than that for most FM metals, giving rise to conductivity mismatch for a FM/-graphene contact (see Chapter 2.2). Previous research has shown a Co/graphene contact with ohmic resistance area product of $R_cA = 65\ \Omega\mu\text{m}^2$, and a spin lifetime $\tau_s = 47$ ps, a diffusion constant $D_S = 0.008\ \text{m}^2\text{s}^{-1}$ and a polarisation $P = 5\%$ at 10 μA current bias and a temperature of 300 K. When introducing TiO_2 as a TB, the ohmic resistance area product increases to $R_cA = 585\ \Omega\mu\text{m}^2$, the spin lifetime to τ_s = 80 ps, while the spin diffusion constant and polarisation does not change for the same current bias and temperature [13]. It is clear that with a much larger ohmic

resistance area product the voltage detection signal would increase, improving the detection efficiency as seen in Figure 2.4.

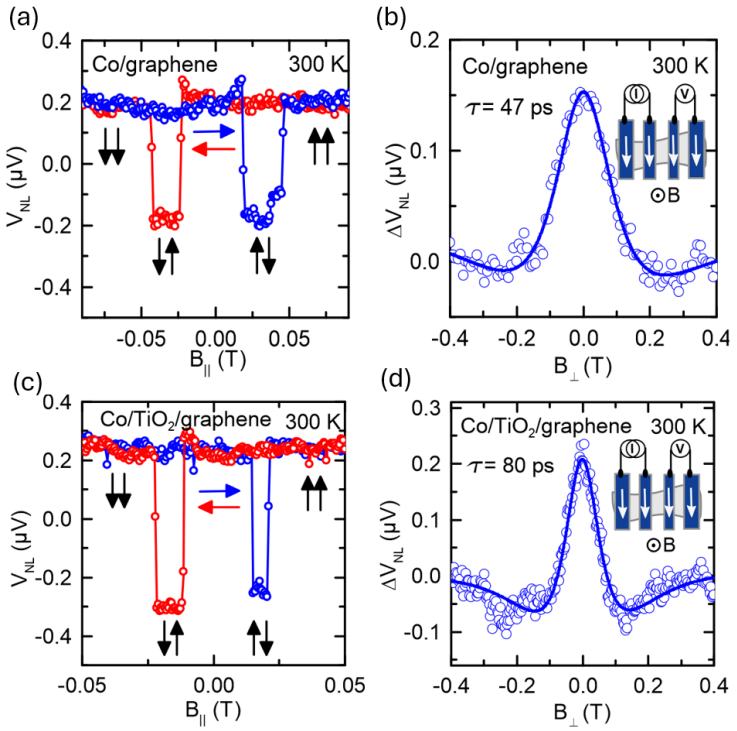

Figure 2.4: Non local spin valve and spin Hanle precession measurements in room temperature at 10 μA bias. (a) Spin valve measurement for Co/graphene contacts lacking a TB. Blue dots are measured with an increasing magnetic field while red dots are measured with a decreasing magnetic field. Black arrows indicate the direction of magnetic domain in the two Co magnetic contacts. Measured spin valve has a $\Delta V_{NL} \approx 0.4$ μV. (b) Spin Hanle precession measurement for Co/graphene contacts lacking a TB. Inset is a figure of the non local measurement setup, along with the direction of magnetic domain in the Co magnetic contacts (white arrows) and the direction of applied field (out of plane). Measurement found a spin lifetime $\tau_s = 47$ ps. (c) Spin valve measurement for Co/TiO_2/graphene contacts. Blue dots are measured with an increasing magnetic field while red dots are measured with a decreasing magnetic field. Black arrows indicate the direction of magnetic domain in the two Co magnetic contacts. Measured spin valve has a $\Delta V_{NL} \approx 0.6$ μV. (d) Spin Hanle precession measurement for Co/TiO_2/graphene contacts. Inset is a figure of the non local measurement setup, along with the direction of magnetic domain in the Co magnetic contacts (white arrows) and the direction of applied field (out of plane). Measurement found a spin lifetime $\tau_s = 80$ ps. Adapted from [13].

It has been shown that a TiO_2 layer on graphene exhibits less large cracks and micro-scale pinholes when compared to an alternative TB (Al_2O_3) layer (see Figure 2.5 (a) and (b)). This leads to lower injection current noise and almost no fluctuations for TiO_2 compared to Al_2O_3 [17], as shown in Figure 2.5 (c) and (d).

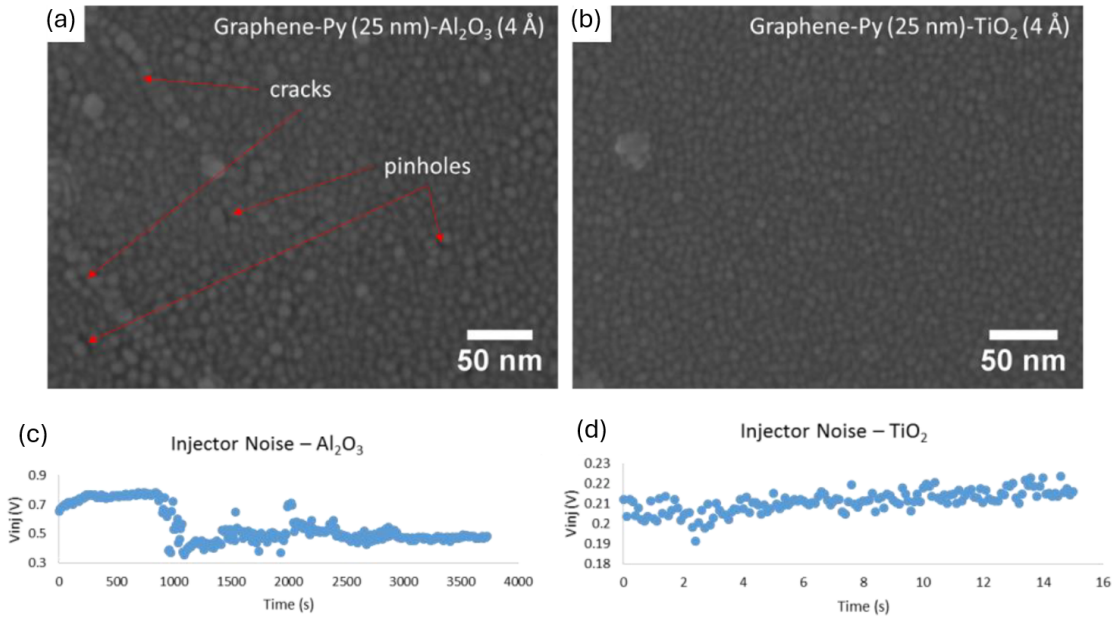

Figure 2.5: Quality of Al_2O_3 and TiO_2 TB for graphene. (a) SEM image of Al_2O_3 TB on top of graphene. Al_2O_3 TB exhibited many cracks and pinholes, indicating possible current leakage through barrier. (b) SEM image of TiO_2 TB on top of graphene. TiO_2 TB did not exhibit as many cracks and pinholes as Al_2O_3 and thus should have a lower current leakage through barrier. (c) Injection noise for Al_2O_3 TB, where measured noise V_{inj} fluctuates between values of 0.3 to 0.7 V. (d) Injection noise for TiO_2 TB, where measured noise V_{inj} is much more stable than the previous case, fluctuating between values of 0.19 to 0.22 V. Adapted from [17].

2.4.2 Spin decay in graphene

The spintronic properties of graphene was first investigated in 2007 by N Tombros *et al.* using exfoliated graphene with cobalt contacts with Al_2O_3 as TB. They found a spin lifetime $\tau_s \approx 100$ ps and a spin diffusion constant $D_S \approx 2.1 \cdot 10^{-2}$ m^2s^{-1} by measuring spin Hanle precession (see Section 3.2.2) [43]. Graphene's low SOC means that spin scattering events by SOC as described in Section 2.3.1 has a weaker effect on graphene, increasing the spin lifetime and spin relaxation length. HF interaction and BAP mechanism has such a weak effect on graphene that they can be negligible, meaning its enough to only consider EY an DP spin scattering mechanisms [8].

In the previous section 2.4.1, it was shown that the spin lifetime is almost twice as large with TiO_2 as TB than without a TB. This combined with no change in spin diffusion constant would increase the spin relaxation length according to Equation (2.13), making spin transport in graphene more efficient when a TB is introduced.

All this has lead to graphene exhibiting a spin relaxation lengths upwards to 30.5 μm at room temperature on exfoliated graphene using Co/MgO contacts and covering the graphene and contacts with hBN [44] and 26.6 μm at room temperature on chemical vapor deposition (CVD) grown graphene using Co/TiO_2 FM contacts and

Ti/Au as reference contacts [9]. This is the longest spin relaxation length measured at room temperature among known materials [8].

3
Experimental

All devices used in this thesis were designed using AutoCAD and fabricated in Myfab Nanofabrication Laboratory at Chalmers. This chapter aims to introduce how these devices were designed and fabricated, as well as introduce the different measurement methods used to produce results.

3.1 Device fabrication

Devices were fabricated on 7 x 7 mm chips that were cut from a wafer of CVD grown graphene on top of Si/SiO_2 by Grolltex Inc. The graphene was then etched into different patterns using electron beam lithography (EBL) to create a mask and O_2-plasma etching to etch away unwanted graphene. Magnetic Co/TiO_2 contacts and non-magnetic Au/Ti contacts were deposited by using EBL to create masks, high vacuum evaporation deposition to deposit metal and a lift-off process to remove unwanted metal deposited. A finished device can be seen in Figure 3.1.

The entire fabrication process is explained in greater details in Appendix A.

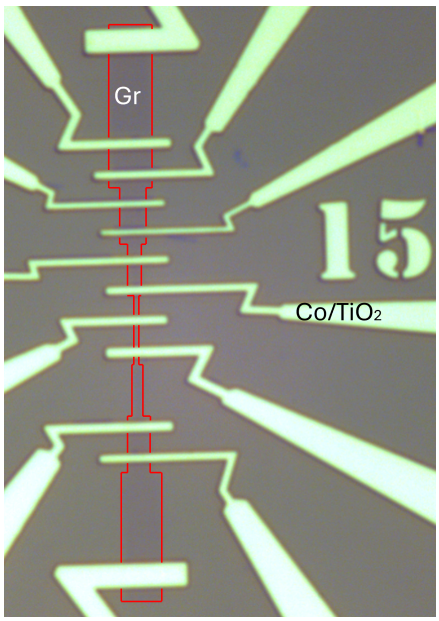

Figure 3.1: Example of a fabricated device with graphene as NM transport layer and Co/TiO_2 FM contacts. The red lines indicate the outline of the graphene channel.

3.2 Measurement techniques

There were two main measurement methods used to detect spin polarised currents for this master's thesis: spin valve and Hanle spin precession. The measurement setup for each type is described in the following sections.

The measurements used a NL four terminal (4T) measurement setup (see Figure 3.2 (a) and (b)). Using a NL measurement setup enables measurement of difference in chemical potential (ΔV_{NL}) from pure spin current (see Figure 3.2 (c)) instead of measuring spin current and charge current as is the case for a local measurement. A 4T measurement setup will only measure the channel and is preferential to a two terminal (2T) measurement setup that would also measure contact and wire resistances. Since both of these measurement methods together enables measurement of the element of interest (pure spin current/voltage) without added contact or wire resistances the measured signal will have a higher signal-to-noise ratio (SNR) [21].

The voltage was measured using a Keithley 2182A nanovoltmeter, The DC bias current and gate voltage were applied using a Keithley 6221 DC current source and Keithley 2450 sourcemeter. The external magnetic field were applied using a GMW 5403 electromagnet.

3.2.1 Non-local spin valve

A general 4T NL spin valve measurement for a graphene/Co device can be seen in Figure 3.2 (a) and (b). Spin current is injected into the graphene through a Co/TiO_2 contact with the same spin direction to the injectors magnetisation and diffuses through the graphene [11]. The diffused spins can be detected by measuring voltage signal at another Co/TiO_2 contact compared to another contact far away from the injector. By defining $x = 0$ at the spin injector, one can solve Equation (2.9) as

$$\mu_{\uparrow\downarrow} = \pm\mu_0 \cdot \exp(-\frac{x}{\lambda_{NM}}) \text{ for } x \geq 0. \tag{3.1}$$

μ_0 is the chemical potential splitting at $x = 0$ and can be expressed as

$$2\mu_0 = e(V_\uparrow - V_\downarrow) = e(I_\uparrow R_\uparrow^{TB} - I_\downarrow R_\downarrow^{TB}) = \frac{eIR_{NM}\gamma_i}{1 + 2\frac{R_{NM}}{R^{TB}}}, \tag{3.2}$$

where γ_i is the spin polarisation at the injectors FM/I/NM interface, I is the total tunnel current, the spin currents through interface is

$$I_{\uparrow\downarrow} = \frac{I}{2} \pm \frac{\mu_0 \sigma_{NM} A}{e\lambda_{NM}} \tag{3.3}$$

and the NM resistance is defined as

$$R_{NM} = \frac{\lambda_{NM}}{\sigma_{NM} A} = R_\square \frac{\lambda_{NM}}{W}, \tag{3.4}$$

where A is the cross section of the injector contact, W is the width of Gr channel and $R_\square$ is the square resistance.

Assuming that only spin current reaches the detector contact, then the detected potential at a distance $x = L$ is

$$\mu_{FM}(L) = \frac{\gamma_d(\mu_\uparrow(L) - \mu_\downarrow(L)) + \mu_\uparrow + \mu_\downarrow}{2}, \tag{3.5}$$

where γ_d is the spin polarisation at the detectors FM/I/NM interface. This potential can be compared to a NM reference contact, which detects a potential

$$\mu_{NM} = \frac{\mu_\uparrow + \mu_\downarrow}{2}. \tag{3.6}$$

Measuring voltage over the detector and reference contacts give rise to a NL voltage

$$V_{NL} = \frac{\mu_{FM} - \mu_{NM}}{e} = \pm\frac{\gamma_i\gamma_d R_\square \lambda_{NM}}{2W}\exp(-\frac{L}{\lambda_{NM}}) \tag{3.7}$$

[13]. V_{NL} can also be measured by comparing the potential at detector contact with another FM reference contact further away from the injector. The reference contact will measure a lower potential since $\mu_{\uparrow\downarrow}$ in Equation (3.5) decreases over distance according to Equation (3.1). As x tends to a value much longer than the spin diffusion length, the spin dependent chemical potential will tend to $\mu_\uparrow = \mu_\downarrow$, which will simplify Equation (3.5) to

$$\mu_{FM} = \frac{\mu_\uparrow + \mu_\downarrow}{2} \tag{3.8}$$

which is very similar to Equation (3.6). Using this contact as reference, one gives rise to NL voltage

$$V_{NL} = \frac{\mu_{FM}(L) - \mu_{FM}(\infty)}{e} = \pm\frac{\gamma_i\gamma_d R_\square \lambda_{NM}}{2W}\exp(-\frac{L}{\lambda_{NM}}), \tag{3.9}$$

which is the same as shown in Equation (3.7).

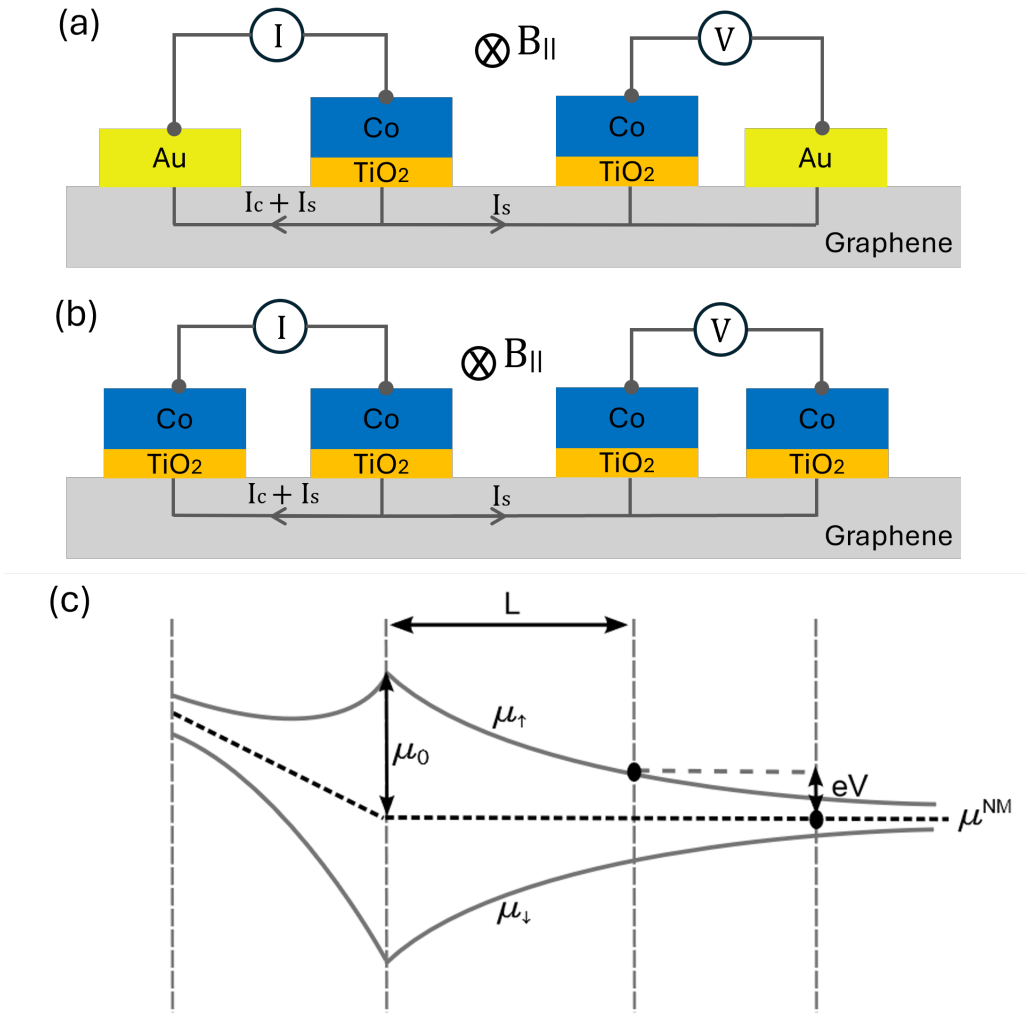

Figure 3.2: Non-local (NL) spin valve. (a) NL spin valve measurement setup with Co/TiO_2 as FM/TB injector and detector contacts, Au as NM reference contact and graphene as NM spin transport. Magnetic field $B_{||}$ is applied parallel to the FM/TB contacts. Charge current I_C propagates through the graphene to the left of injector contact in a closed circuit on the left side of the device, while spin current I_S diffuses to both sides of the injector contact. The detector contact on the right side of the device will therefore only detect chemical potential given by the spin current I_S and compare it to the potential from a NM Au contact. This gives rise to the NL voltage V_{NL} shown in Equation (3.7). (b) NL spin valve measurement setup with Co/TiO_2 as FM/TB injector, detector and reference contacts, and graphene as NM spin transport. Magnetic field $B_{||}$ is applied parallel to the FM/TB contacts. Charge current I_C propagates to the left of injector contact in a closed circuit on the left side of the device, while spin current I_S diffuses to both sides of the injector contact. The detector contact on the right side of the device will therefore only detect chemical potential given by the spin current I_S and compare it to a lower potential given by the spin current I_S at the reference contact. This gives rise to the NL voltage V_{NL} shown in Equation (3.9). (c) The electrochemical potential in the NM graphene layer. As spins diffuse through the graphene, the chemical potential for different spins will be split into and measured chemical potential will be different for different distances from injector contact. Adapted from [13].

Since a rectangular contact tends to only have magnetisation in two directions due to easy axis alignment and the required magnetic field to change direction is dependent on the width of the contact (see section 2.2.1), these directions can be labelled as up ($\uparrow$) and down ($\downarrow$) for each contact. As long as both the injector and detector contacts does not have the same width, it is possible to find a magnetic field where these are either parallel ($\uparrow\uparrow$ or $\downarrow\downarrow$) or anti parallel ($\uparrow\downarrow$ or $\downarrow\uparrow$). To measure NL spin valve, a in plane magnetic field $B_{||}$ is applied and swept in both directions to measure V_{NL} for these 4 states. When sweeping from a negative magnetic field to a positive one, both contacts will start in a parallel state (*e.g.* $\uparrow\uparrow$) and then at a certain magnetic field one of the contacts will 'flip' and the device transitions into an anti parallel state (*e.g.* $\uparrow\downarrow$), then the other contact will 'flip' and the state transitions back into a parallel state with opposite direction to the parallel state it started with (*e.g.* $\downarrow\downarrow$). When sweeping the magnetic field in the opposite direction, from positive field to negative, the contacts will 'flip' in the opposite direction (*e.g.* state goes from $\downarrow\downarrow$ to $\downarrow\uparrow$ to $\uparrow\uparrow$). One has therefore managed to measure V_{NL} in all 4 possible states. An example of a spin valve signal in graphene using Co/Al_2O_3 contacts can be seen in Figure 3.3 (b).

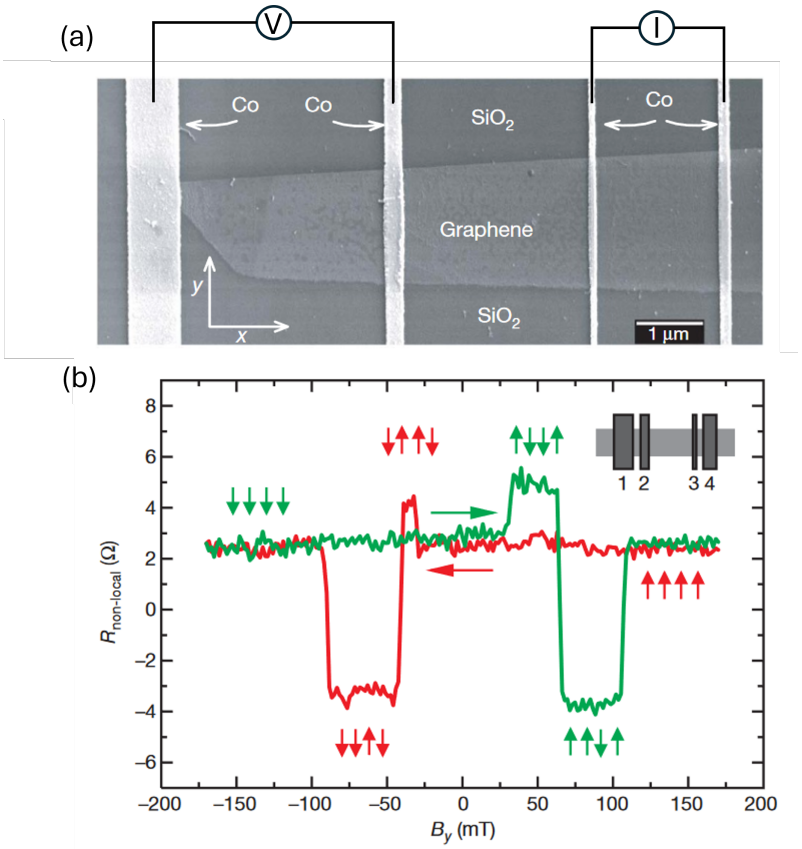

Figure 3.3: Non-local spin valve measurement. (a) Scanning electron microscopy (SEM) image of measured device along with the non-local measurement setup. Device consists of a single layer graphene flake on top of SiO_2 chip with Co/Al_2O_3 injector, detector and reference contacts. Adapted from [43]. (b) Non local spin valve measurement. Magnetic field is swept from negative to positive (green) and positive to negative (red), the arrows above indicate the magnetisation of contact 1, 2, 3 and 4 where contact 1 and 4 is reference contacts, contact 2 is detector and contact 3 is injector. Note that reference contacts are included here as they are not far enough away to assume negligible magnetic flip contribution and hence the simplification in Equation (3.8) cannot be made. There are clear peaks measured when detector and injector are anti parallel. Adapted from [43].

3.2.2 Non-local Hanle spin precession

NL Hanle spin precession is measured by using the 4T measurement setup shown in Figure 3.4 (a) and applying a magnetic field $B_\perp$ perpendicular to the spin transport channel. The applied field will cause spin precession with the Larmor frequency

$$\omega_L = \frac{g\mu_B B_\perp}{\hbar} \tag{3.10}$$

where g is the Landé g-factor, μ_B the Bohr magneton and $\hbar$ the reduced Planck's constant [15]. During diffusion, the spin precession decreases the spin accumulation at injector contact for low magnetic fields, while coherent decaying oscillations occurs at large magnetic fields [45]. The reduction of spin accumulation can be detected

by the reduction of voltage in Equation (3.9). Since spins diffuses randomly, and scattering and spin flips occurs, the probability of a spin diffusing and preserving its spin state at a contact at distance x from the injector ($x = 0$) after time t is

$$P(x,t) = \underbrace{\sqrt{\frac{1}{4\pi D_s t}}\exp(-\frac{x^2}{4D_s t})}_{1}\underbrace{\exp(-\frac{t}{\tau_s})}_{2} \tag{3.11}$$

where D_S is the spin diffusion constant, τ_s is the average spin lifetime, (1) describes spin diffusion and (2) spin dephasing.
The potential $\mu(x, B_\perp) = \int_0^\infty \mu(x, B_\perp, t)dt$ is a sum of all spins injected over all diffusion times. By setting the boundary condition $\mu(0, 0) = \mu_0$, the potential can be written as

$$\mu(x, B_\perp) = 2\sqrt{\frac{D_s}{\tau_s}}\int_0^\infty P(x,t)\cos[\omega_L(B_\perp)t]dt. \tag{3.12}$$

By combining Equation (3.12) with (3.2) and (3.9), the detected voltage signal at a detector with distance $x = L$ from injector can be written as

$$V_{NL}(L, B_\perp) = \pm\frac{\gamma_i\gamma_d R_\square I}{W}\int_0^\infty \underbrace{\sqrt{\frac{D_s}{4\pi t}}\exp(-\frac{L^2}{4D_s t})}_{1}\underbrace{\cos[\omega_L(B_\perp)t]}_{2}\underbrace{\exp(-\frac{t}{\tau_s})}_{3}dt \tag{3.13}$$

where the factors in integral originates from spin diffusion (1), spin precession (2) and spin dephasing (3). V_{NL} will have different signs depending on if the injector and detector contacts magnetisation's are parallel or anti parallel [13]. Measured Hanle signals can be fitted using Equation (3.13) to extract parameters such as spin diffusion D_S and spin lifetime τ_s that can be used to calculate spin relaxation length λ_S using Equation (2.13). An example of a Hanle spin precession measurement and data fit can be seen in Figure 3.4 (b).

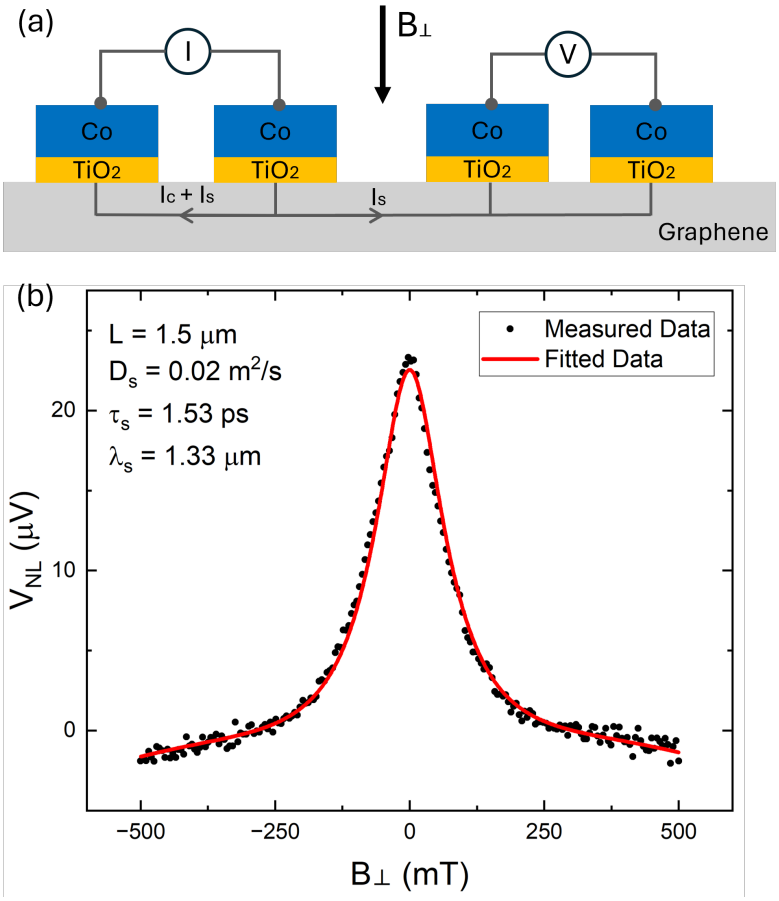

Figure 3.4: Non-local Hanle spin precession. (a) Non-local Hanle spin precession measurement setup with Co/TiO_2 FM/TB injector, detector and reference contacts with graphene as spin transport layer. Charge current propagates from the injector contact to the left reference contact to form a closed loop, while injected spin current will diffuse to both sides of injector contact. The spins will precess while diffusing due to the applied perpendicular magnetic field. Since diffusion is random, the detected spins at detector contact will carry different spin and the detected signal will be the average spin. (b) Measured non-local Hanle spin precession. Black dots is data as measured while red line is the data fitted to Equation (3.13) by setting $g = 2$ and $L = 1.5$ μm. With the fitted equation, parameters D_S, τ_s and λ_S were extracted to be 0.02 m^2/s, 1.53 ps and 1.33 μm.

3.2.2.1 Symmetric and antisymmetric Hanle signals

Hanle signals can either be symmetric or antisymmetric (asymmetric) around the point $B_\perp = 0$ or a combination of both (see Figure 3.5). The measured signal V_{NL} only measures spin current that is either parallel (P) (positive voltage) or anti parallel (AP) (negative voltage) with the FM detectors magnetisation. If the injected spin current is P or AP the detector will measure a peak at $B_\perp = 0$ that will decrease at the same rate as the magnetic field increases independent of magnetic field direction. If the injected spin current is instead injected with a perpendicular direction to the FM detectors then the spin current will have no component in P

or AP direction and hence no signal will be measured at $B_\perp = 0$. As an external magnetic field is applied the spin will precess in either P or AP direction depending on the direction of magnetic field and the signal will increase (for P direction) or decrease (for AP direction) at the same absolute rate as magnetic field strength increases. Hence a symmetric (asymmetric) signal can only occur if the spin current is injected P or AP (perpendicular) to the FM detectors magnetisation. If the spin current is injected with an angle, then the Hanle signal will be a combination of symmetric and asymmetric signal and this angle can be measured. This was done by measuring Hanle signals for when the detector and injector FM magnetisation is P and AP. The measured Hanle signal will have opposite sign for P and AP according to Equation (3.13). To eliminate non-spin related background noise, the average of both signals

$$V_{NL,Avg} = \frac{V_{NL,P} - V_{NL,AP}}{2} \tag{3.14}$$

was calculated, where $V_{NL,P}$ is the voltage for parallel magnetisation and $V_{NL,AP}$ for anti parallel. The average signal was then decomposed into its symmetric and asymmetric components using equations:

$$\begin{cases} V_{NL}^{||} = \dfrac{V_{NL,Avg}(B) + V_{NL,Avg}(-B)}{2} \\ \\ V_{NL}^{\perp} = \dfrac{V_{NL,Avg}(B) - V_{NL,Avg}(-B)}{2}, \end{cases} . \tag{3.15}$$

where $V_{NL}^{||}$ is the symmetric component and $V_{NL}^{\perp}$ is the asymmetric component. These can then be fitted using equations

$$\begin{cases} V_{NL}^{||} \propto \displaystyle\int_0^\infty \frac{1}{\sqrt{4D_s t}} \exp(-\frac{L^2}{4D_s t}) \cos(\omega_L t) \exp(-\frac{t}{\tau_s}) dt \\ \\ V_{NL}^{\perp} \propto \displaystyle\int_0^\infty \frac{1}{\sqrt{4D_s t}} \exp(-\frac{L^2}{4D_s t}) \sin(\omega_L t) \exp(-\frac{t}{\tau_s}) dt. \end{cases} . \tag{3.16}$$

The symmetric and asymmetric amplitudes $\Delta V_{NL}^{||}$ and $\Delta V_{NL}^{\perp}$ can then be extracted and used to calculate the angle φ between injected spin polarization and FM detectors magnetisation direction by

$$\varphi = \tan^{-1}(\frac{\Delta V_{NL}^{\perp}}{\Delta V_{NL}^{||}}) \tag{3.17}$$

[46].

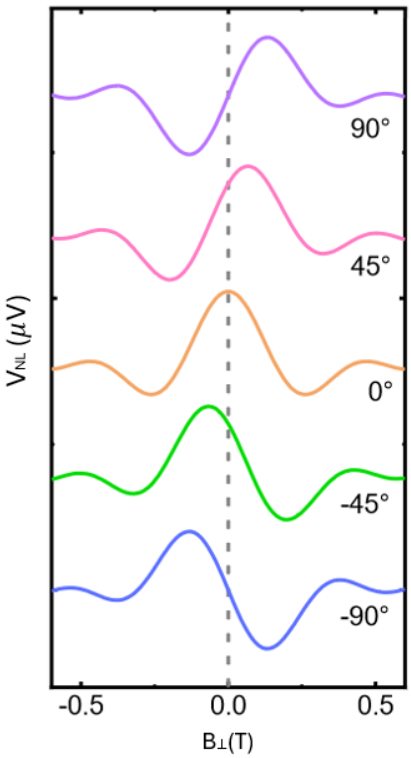

Figure 3.5: Simulation of Hanle signal for different angles between injected spin current and FM detector magnetisation direction. At 0° the signal is symmetric around $B_\perp = 0$, at ±90° the signal is asymmetric around $B_\perp = 0$ and at ±45° the signal is a combination of symmetric and asymmetric compounds. Adapted from [46].

4
Results

Since the discovery of graphene by Geim and Novoselov [47], its unique properties has shown great potentials in many areas and therefore gained plenty of attention. For spintronics, graphene's exceptional high carrier mobility and weak intrinsic spin-orbit coupling has lead to a long spin diffusion length and spin lifetime, two properties with extreme importance for spin transport [48]. Here, we tried to push the limit of graphene spintronics by examining spin transport properties while spin transport layer is constrained by small channel width and investigated how spin transport is affected by such constrained geometries. The examination was done by NL spin valve and NL Hanle spin precession measurements at room temperature.

4.1 Non-local spin transport

NL spin valve measurements were conducted to measure the devices spin transport parameters. The NL measurement setup used can be seen in Figure 4.1 (a) and a fabricated device in Figure 4.1 (b).

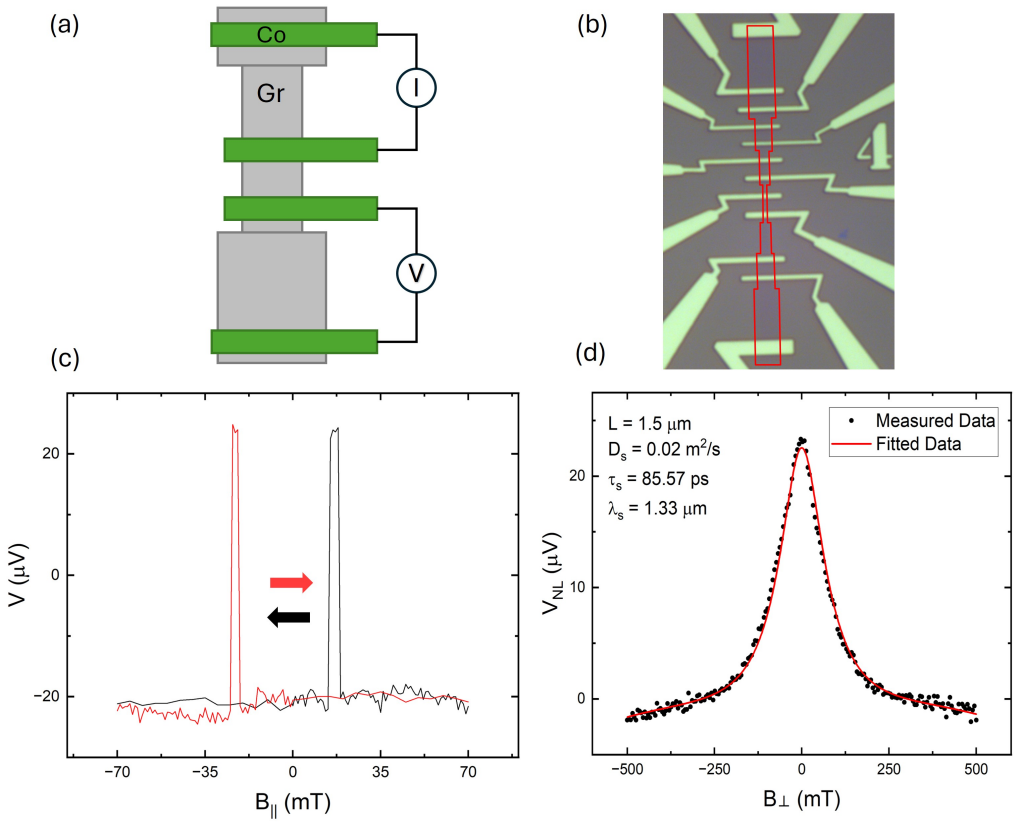

Figure 4.1: NL spin valve and Hanle measurements. (a) Schematic of measurement setup where the green contacts are Co/TiO_2 FM contacts and the grey areas are graphene used as transport layer. (b) Microscopic image of measured device, where Co/TiO_2 is shown in green and graphene as a darker shade of grey outlined in red lines. (c) NL spin valve measurement for a current bias $I = -100$ μA. Red (black) indicates measured spin signal V_{NL} when magnetic field is swept in a positive (negative) direction. (d) NL Hanle measurement for a current bias $I = -100$ μA. Black dots indicate measured V_{NL} while red line is the measured data fitted to Equation (3.13). Using the fitted line, parameters $D_S = 0.02$ m^2/s, $\tau_s = 85.57$ ps and $\lambda_S = 1.33$ μm were extracted.

NL spin valve was measured at different current bias, where each measurement had a fixed current bias while sweeping an applied magnetic field between -70 to 70 mT. Figure 4.1 (c) shows the NL spin valve measurement for a fixed current bias of $I = -100$ μA, where the red (black) line was measured while sweeping applied magnetic field from -70 to 70 (70 to -70) mT. The results shows two clear low noise peaks when the magnetic contacts switches from P to AP magnetisation (see Section 3.2.1 for details). The two peaks has an average $\Delta V_{NL} = 44.7 \pm 1$ μV which is large indicating a high polarisation of the FM contacts, effective spin injection and excellent spin transport across the graphene spin channel.

NL Hanle measurements were conducted afterwards for current biases in devices which showed NL spin valve signals. For the Hanle measurements, the applied magnetic field was rotated to out of plane (90°) and swept between -500 to 500 mT.

Figure 4.1 (d) shows the NL Hanle measurement for a current bias of $I_B = -100$ μA, where the black dots are data as measured and the red line is the measured data fitted to Equation (3.13). Using the fitted line, it was possible to extract $D_S = 0.02$ m^2/s, $\tau_s = 85.57$ ps and $\lambda_S = 1.33$ μm. The fitted line follows the measured data well indicating a good fit with low SNR and unambiguously confirm the excellent measured spin characteristics.

A spin lifetime $\tau_s = 85.57$ ps and a spin diffusion length $\lambda_S = 1.33$ μm is quite low compared to a paper submitted by M. Drögeler *et al.* [44] where a single layer graphene encapsulated in hBN extracted $\tau_s = 12.6$ ns and $\lambda_S = 30.5$ μm. However, this is expected as the hBN flakes will cover the graphene and keep it perfectly flat, preventing doping from the substrate and solvents from interacting with the graphene layer. This is important as dopants and solvents has been shown to significantly reduce the spin lifetime below 1 ns [44]. The extracted values are however, relatively good when compared to another paper submitted by N. Tombros *et al.* [43] who measured $\tau_s = 155$ ps and $\lambda_S = 1.6$ μm on single layer graphene flakes in RT with Co/Al_2O_3 FM contacts. These devices are similar to device shown in Figure 4.1 (b) with the notable exception of Al_2O_3 used as TB (for this report TiO_2 were used) and exfoliated graphene used to create the single graphene layer (for this report CVD graphene were used). Al_2O_3 as TB leads to higher injection current noise and more fluctuations compared to a TB using TiO_2 (see Section 2.4.1). Exfoliated graphene flakes has better quality than that of a CVD grown graphene layers and is the more significant source to the difference in spin characteristics, however it is not scalable like CVD graphene is. When comparing to papers submitted by A. Avsar *et al.* [49], M. Wojtaszek *et al.* [26], W. Fu *et al.* [50], A. L. Friedman *et al.* [51] whom all measured $\tau_s \approx 80 - 285$ ps and $\lambda_S \approx 1.1 - 1.5\mu$m for CVD grown graphene. It is worth to note that the spin lifetime τ_s measured above 200 ps in papers mentioned are either bi-layer graphene (BLG) [49] while this thesis uses single-layer graphene (SLG) or uses BN as a TB [50] while this thesis uses TiO_2 as TB. It can therefore be noted that the extracted parameters seem reasonable when compared to previous research done within the field. The data measured from Figure 4.1 (c) and (d) can therefore be used as generic examples of good spin valve and Hanle signals.

4.2 Current bias dependence

NL spin valve measurements for different current bias were conducted to characterise the devices current bias dependence. The results present here were all measured on the same device as above (see Figure 4.1 (a) and (b)).

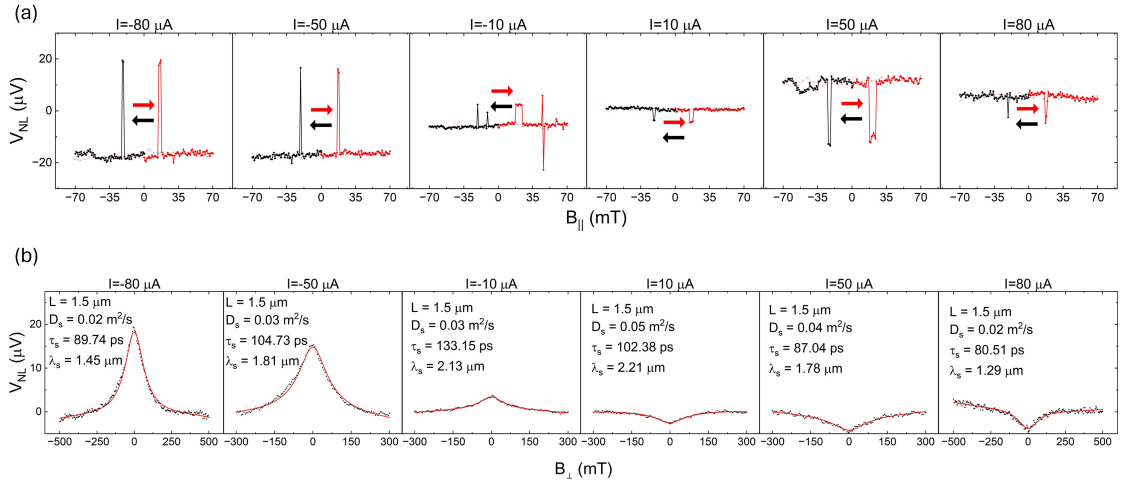

Figure 4.2: Spin signals current dependence for device shown in Figure 4.1. (a) NL spin valve measurements for different current biases I_B = -80, -50, -10, 10, 50, 80 μA. Red (black) indicates measured spin signal V_{NL} when magnetic field is swept in a positive (negative) direction. Note all figures share the same y-axis. (b) NL Hanle measurements for different current bias. Black dots indicate measured V_{NL} while red line is the measured data fitted to Equation (3.13). Using the fitted line, parameters D_S, τ_s and λ_S were extracted with values shown in Figure. Note, all figures share the same y-axis.

Figure 4.2 (a) shows spin valve measurements for different current biases. It is noted that the peak ΔV_{NL} is heavily dependent on current bias, where a larger current will increase ΔV_{NL} and current in opposite directions will flip the peak. This current bias dependence is expected to be linear [48] which corresponds with measurements done in this project. The only notable exception is $|\Delta V_{NL}|$ for $I_B = 50$ μA is larger than $|\Delta V_{NL}|$ for $I_B = 80$ μA. This result can be due to many factors such as degradation of device affecting the sheet resistance of graphene layer, change in oxide TB changing the contact resistance, or hot-electron effects [52]. However, the reason behind this is out of scope for this project and will not be further discussed.

Hanle signal peaks as shown in Figure 4.2 (b) indicate a strong current bias dependence similar to the case of spin valve above. This linear dependence is expected as per previous research in the field [53]. It is however noted that, even with a current bias dependent peak, the extracted parameters do not exhibit such a dependence. This can be explained from Equation (3.13), where the peak has its current dependence outside of the infinite integral. When using the equation to extract the parameters inside the integral, everything outside of the integral is assumed to be a constant (which is the case for a constant current bias). Since there is no current in-

side of the integral and the parameters themselves are not current dependent, theory says that there should be no current dependence when extracting the parameters. Additionally, the spin transport parameters are dependent on the properties of the spin transport channel, which are independent of the spin current. This can be seen in Figure 4.5 where λ_S, D_S and τ_s seem to not change with changing current bias.

4.3 Width dependence

Spin valve and Hanle measurements were done for devices with different graphene width in order to investigate width dependence. Since some of the devices were designed with FM contacts attached to different graphene widths, it was possible to measure both uniform width (See Figure 4.3 (a)) and non-uniform width (see Figure 4.3 (b)) where the graphene width changed along the channel.

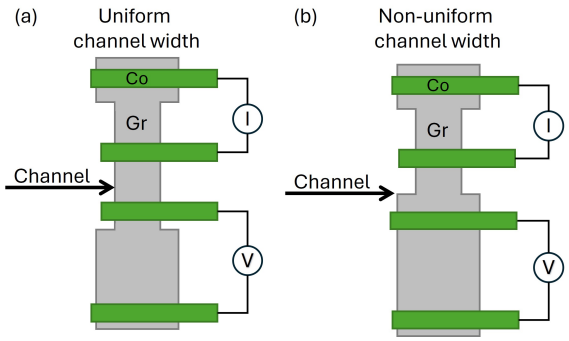

Figure 4.3: Device geometry for (a) uniform channel width devices and (b) non-uniform channel width devices. The grey area is graphene as transport layer, the green contacts are Co/TiO_2 FM contacts and the channel is highlighted by an arrow.

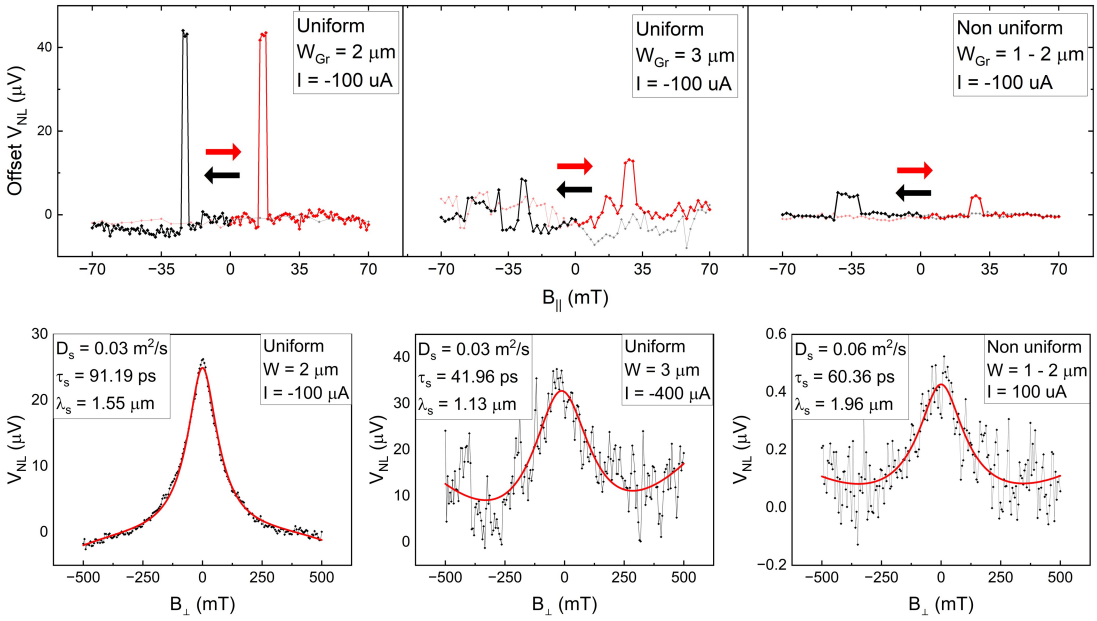

Figure 4.4: Spin signals graphene width dependence. (a) NL spin valve measurements for uniform graphene width 2 μm, 3 μm and non uniform where one contact has width 1 μm and the other 2 μm. Red (black) indicates measured spin signal V_{NL} when magnetic field is swept in a positive (negative) direction. Note all figures share the same y-axis. (b) NL Hanle measurements for uniform graphene width 2, 3 μm and non uniform where one contact has width 1 μm and the other 2 μm. Black dots indicate V_{NL} as measured while red line is the measured data fitted to Equation (3.13). Using the fitted line, parameters D_S, τ_s and λ_S were extracted with values shown in inset.

Spin valve measurements for different channel widths with the same channel length is shown in Figure 4.4 (a) and Hanle measurements for different widths in Figure 4.4 (b). It is clear that the 2 μm wide uniform graphene strip showed the best results as it is less noisy, the spin valve has a bigger peak ($\Delta V = 19.1 \pm 0.2$ μV) than the others and the fitted line follows the measured data far better than for the others. This result could be due to many factors such as the contacts spin polarisation, contact resistance, impurities or residues around the graphene affecting the properties of graphene, impurities or holes in TB and fabrication errors causing unwanted geometry. Due to limited time and resources, none of these factors could be studied in detail and it is therefore impossible to know exactly which factors affected the result. However, it is still possible to argue that edge scattering decreases the spin performance for the non uniform sample. This is due to edge scattering increasing the likelihood of spin flip to occur [54] and by changing the width between contacts, more edges are introduced increasing the probability of edge scattering affecting the spin current. This could explain why the spin valve for non uniform sample, while having as little noise as the uniform 3 μm sample, still has a small peak ($\Delta V = 0.4 \pm 0.1$ μV) compared to the uniform samples. This same argument can however, also be used to conclude that a smaller width of graphene should increase the probability of edge scattering and therefore decrease the spin transport

properties. This is however not the case between the 2 and 3 μm measurements shown in Figure 4.4, where the 2 μm sample outperforms 3 μm. Possibly, these widths are still large enough for the edge scattering effects to not make a big impact as the widths are still larger than extracted spin diffusion lengths, or other non determined factors mentioned earlier has a far greater effect on the result which results in the 2 μm sample performing far better than the 3 μm sample.

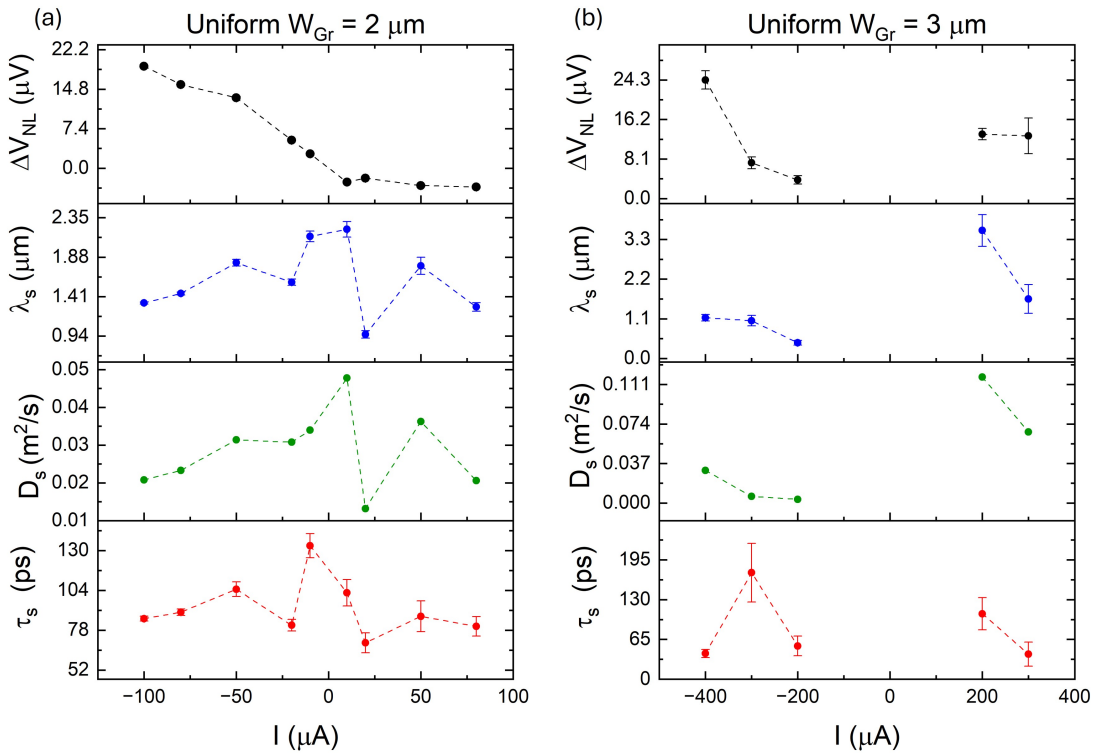

Figure 4.5: Spin parameters current dependence for different widths. Spin parameters ΔV_{NL}, λ_S, D_S and τ_s for different current bias were extracted from Hanle measurements using a line fitted to Equation (3.13) for (a) 2 μm wide graphene strip and (b) 3 μm wide graphene strip.

The spin parameters extracted for 2 and 3 μm wide graphene strips are shown in Figure 4.5 (a) and (b), respectively. The figure shows a clear current dependence for ΔV_{NL} and no current dependence for any other spin parameters which aligns with results mentioned in Section 4.2. This pattern is however not the case around $I = 0$ μA, where all spin parameters seem to deviate from any other measurements for other currents. This is the case since such low current decreases SNR making it more prone to deviations from noise. The uniform 3 μm measurements in Figure 4.5 (b) has such low SNR that no signals could be detected due to the high noise. Due to this, measurements around $I = 0$ μm are not of much interest for analysis, it is evidentially better to analyse measurements with larger currents. However, when analysing measurements at higher currents it cannot be determined how much the width affects the current bias (or lack of) dependence for parameters due to lack of data. More measurements of different widths would be needed to determine this.

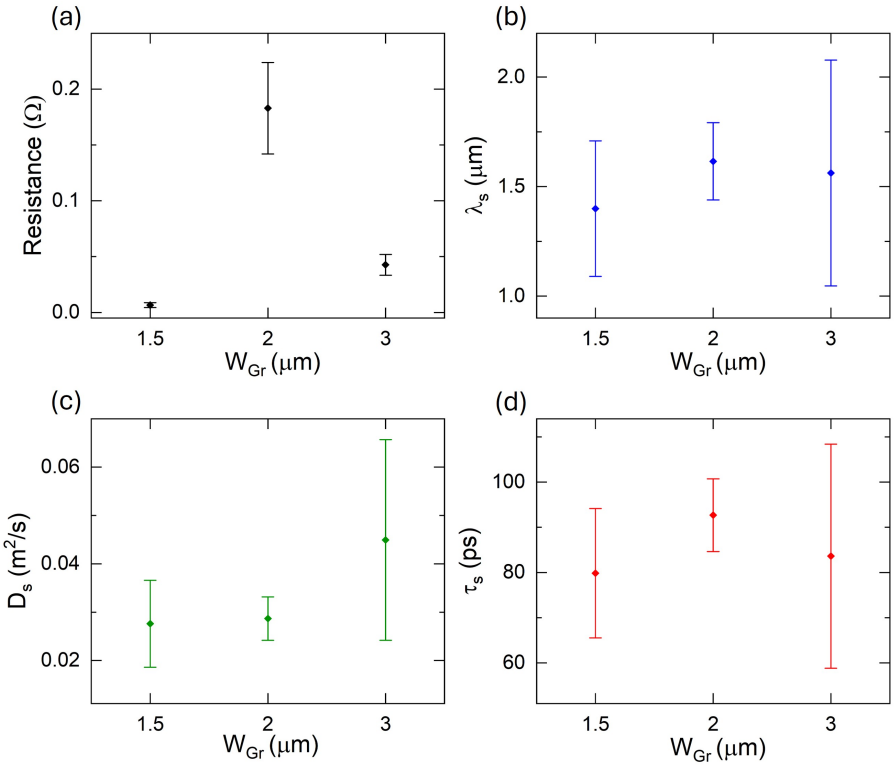

Figure 4.6: Spin parameters width dependence for (a) NL resistance $\frac{V_{NL}}{I}$, (b) spin diffusion length λ_S, (c) spin diffusion D_S and (d) spin lifetime τ_s. The dot in the middle is the average value from different devices and different current biases given a width while the error bars shows the 95% confidence interval of variation for a given width. $W_{Gr} = 1.5$ μm is the non-uniform 1 - 2 μm graphene strip while $W_{Gr} = 2$ μm and $W_{Gr} = 3$ μm are uniform graphene strips.

Figure 4.6 shows the width dependence for different NL spin parameters by summarizing the NL spin parameters extracted from different devices and different current bias. There does not seem to be any trends for any parameters by looking at the width dependence. However, this may be the case due to small sample size and I therefore argue that further studies need to be conducted in order to conclude anything of significance. Figure 4.6 (a) shows that the width 2 μm has a much larger spin signal than all other widths. However, this width also shows a large variation in error bars. The cause of this variation should not be due to current bias since resistance is calculated by dividing the NL voltage by the bias current, hence removing the current dependence. It is therefore more likely to be due to the quality of graphene from different devices, impurities, contact polarisation and contact resistance that causes a variation in ΔV_{NL} for the same bias current and hence a variation in resistance. This hypothesis is further supported by analysing the error bars for the other spin parameters in Figure 4.6 (b), (c) and (d). These spin parameters are not bias current dependent as discussed in Section 4.2 and hence their error bars are caused by other factors like the quality of graphene from different devices, impurities, contact polarisation and contact resistance. These variations are so large that one can draw a horizontal line across any of the spin parameters

apart from the resistance and be within the 95% confidence interval for all widths, rendering it impossible to argue for any width dependence. However, as mentioned before it is also not reasonable to argue for no width dependence due to the small sample size and hence the only conclusion made from this is that further studies need to be conducted using a larger sample size.

4.4 Hanle spin angle

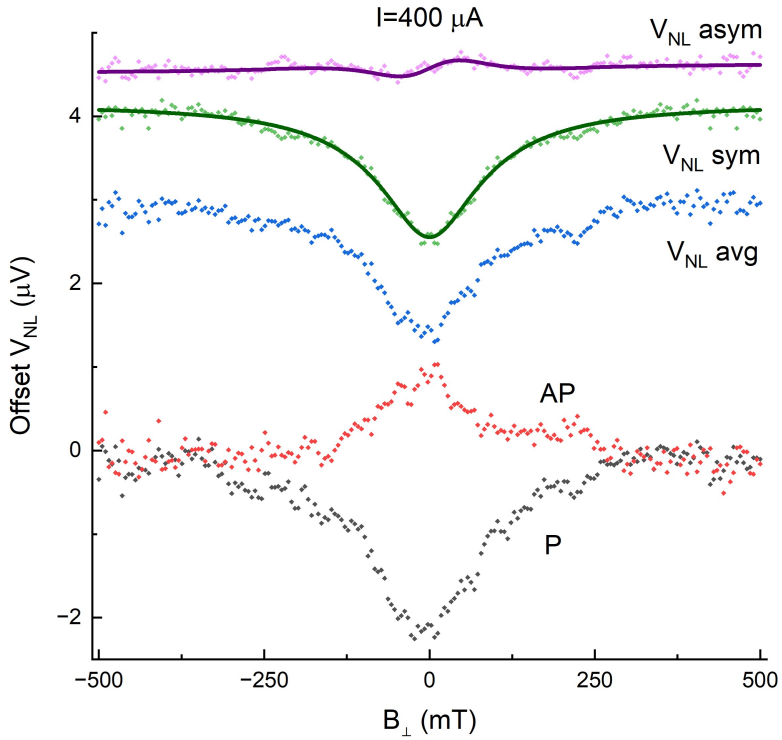

Figure 4.7: Symmetric and asymmetric Hanle signals for current bias $I = 400\ \mu$A. Black (red) dots indicates measured parallel (anti parallel) Hanle signals. Blue dots indicate the average Hanle signal of parallel and anti parallel calculated according to Equation (3.14). Green (purple) dots indicate the symmetric (asymmetric) components of the average Hanle signal calculated using Equation (3.15) and its respective solid line is the data fitted to Equation (3.16).

Figure 4.7 shows Hanle signals when injector and detectors magnetisation is P and AP which has different directions in amplitude, as proposed by Equation (3.13). These signals were used to calculate an average using Equation (3.14) to remove any signal background and plotted in Figure 4.7. The average signal was then decomposed into its symmetric and asymmetric components using Equation (3.15), fitted to Equation (3.16) and plotted in Figure 4.7. The amplitude of the symmetric component is very large in comparison to the asymmetric, indicating a low angle between the spin current injection and detector magnetisation direction. This is expected as the devices were designed with parallel contacts and symmetric signal

arise from spin current parallel to contacts while asymmetric arise from spin current perpendicular to contacts. The Hanle spin angle was calculated to be $\varphi = 4.8 \pm 0.8°$ by using Equation (3.17) and the amplitudes for symmetric and asymmetric components in from Figure 4.7. With such a small angle, the asymmetric component should not affect the spin measurements by any significant factor and can therefore be neglected.

4.5 Suggestion for future work

The research conducted for this project would require future work to draw any significant conclusions. Here I present some points of improvements for future work.

(1.) More measurements would enable a more in depth analysis which could provide a better understanding of the width dependence and may also enable a statistical analysis. One way to do this is to improve the fabrication method to find a more reliable recipe for spintronic devices. Such an improvement could be to purchase or grow higher quality graphene as the results shown above hints at low graphene quality or to find a better development process to reduce imperfections and increase overall device quality.

(2.) It could be interesting to investigate fabrication methods such as parameters for EBL to create higher resolution exposures to fabricate devices with smaller channel width, channel length and contact width. However, as this would add more complexity to the project it might be deemed better to first complete experiments on larger devices before trying to minimize sizes even further.

(3.) It could also be interesting to look at different shapes of contacts such as a circular contacts for applications such as Heisenberg machines as suggested by Bunaiyan *et al.* [55]. Current problem for circular contacts is to design a sufficient small circular contact with extended contacts connecting it to bonding pads.

5
Conclusion

NL spin valve and NL Hanle precession was measured for devices fabricated and the measurements showed large peaks indicating a high polarisation of the FM contacts, low SNR, excellent spin transport characteristics. Upon investigating current bias dependence, it was concluded that ΔV_{NL} is linearly dependent on current bias while the extracted spin parameters λ_S, D_S and τ_s showed no current bias dependence.

It has been demonstrated that NL spin measurements was achieved for uniform 2 and 3 μm and non-uniform $1-2$ μm wide graphene strips with average spin diffusion length (λ_S) 1.59 μm for uniform and 1.4 μm for non-uniform, average spin diffusion (D_S) 0.04 m^2/s for uniform and 0.03 m^2/s for non-uniform, and average spin lifetime (τ_s) 88.15 ps for uniform and 79.84 ps for non-uniform. A uniform graphene strip showed better spin current performance, less noise and larger peaks compared to non uniform graphene strips, most likely due to increased edge scattering in non uniform strips as discussed in Section 4.3. The biggest peak ($\Delta V_{NL} = 44.7 \pm 1$ μV) in spin valve and Hanle measurements were achieved with a uniform 2 μm wide graphene strip with current bias $I = -100$ μA and spin parameters with $\lambda_S = 1.33$ μm, $D_S = 0.02$ m^2/s and $\tau_s = 85.57$ ps.

When examining the spin parameters width dependence, no significant conclusion could be drawn. All measurements show too much variation rendering it impossible to determine any trends in data points. With further studies, one could gather more measurements and may find a trend one could draw a conclusion from.

Measuring one of the devices Hanle spin angle it was calculated to be $\varphi = 4.8 \pm 0.8°$. As this is a very low angle it was concluded that the angle between injection and detection to not be a determining factor to the lack of measurable devices.

Bibliography

[1] "A history of the invention of the transistor and where it will lead us," ResearchGate, Oct. 2024, doi: 10.1109/4.643644.

[2] "The History of the Component of the Logic Gates," in 2017 6th International Conference on Advanced Materials and Computer Science (ICAMCS 2017), Clausius Scientific Press Inc., 2017.

[3] "Frontier development of chips design and production," ResearchGate, Oct. 2024, doi: 10.1016/j.procs.2018.10.232.

[4] I. Žutić, J. Fabian, and S. Das Sarma, 'Spintronics: Fundamentals and applications', Rev. Mod. Phys., vol. 76, no. 2, pp. 323–410, Apr. 2004, doi: 10.1103/RevModPhys.76.323.

[5] S. Bandyopadhyay and M. Cahay, "Introduction to Spintronics. 2nd ed.", Boca Raton, Florida: CRC Press, 2016. isbn: 978-1-4822-5557-7.

[6] A. K. Geim and K. S. Novoselov, "The rise of graphene," Feb. 26, 2007, arXiv: arXiv:cond-mat/0702595. doi: 10.48550/arXiv.cond-mat/0702595.

[7] "It's still all about graphene," Nature Mater, vol. 10, no. 1, pp. 1–1, Jan. 2011, doi: 10.1038/nmat2938.

[8] A. Avsar, H. Ochoa, F. Guinea, B. Özyilmaz, B. J. van Wees, and I. J. Vera-Marun, "Colloquium: Spintronics in graphene and other two-dimensional materials," Rev. Mod. Phys., vol. 92, no. 2, p. 021003, Jun. 2020, doi: 10.1103/RevModPhys.92.021003.

[9] D. Khokhriakov, B. Karpiak, A. Md. Hoque, and S. P. Dash, "Two-dimensional spintronic circuit architectures on large scale graphene," Carbon, vol. 161, pp. 892–899, May 2020, doi: 10.1016/j.carbon.2020.01.103.

[10] S. Roche et al., 'Graphene spintronics: the European Flagship perspective', 2D Mater., vol. 2, no. 3, p. 030202, Jul. 2015, doi: 10.1088/2053-1583/2/3/030202.

[11] D. Khokhriakov, "Graphene spin circuits and spin-orbit phenomena in van der Waals heterostructures with topological insulators".

[12] N. F. Mott and R. H. Fowler, 'The electrical conductivity of transition metals', Proceedings of the Royal Society of London. Series A - Mathematical and Physical Sciences, vol. 153, no. 880, pp. 699–717, Jan. 1997, doi: 10.1098/rspa.1936.0031.

[13] A. Dankert, M. Venkata Kamalakar, A. Wajid, R. S. Patel, and S. P. Dash, "Tunnel magnetoresistance with atomically thin two-dimensional hexagonal boron nitride barriers," Nano Res., vol. 8, no. 4, pp. 1357–1364, Apr. 2015, doi: 10.1007/s12274-014-0627-4.

[14] F. J. Jedema, Electrical spin injection in metallic mesoscopic spin valves. in MSC Ph.D.-thesis series, no. 2002,8. Groningen: Materials Science Centre, 2002.

[15] M. H. D. Guimaraes, "Spin and Charge Transport in Graphene Devices in the Classical and Quantum Regimes".

[16] R. J. Soulen et al., "Measuring the Spin Polarization of a Metal with a Superconducting Point Contact," Science, vol. 282, no. 5386, pp. 85–88, Oct. 1998, doi: 10.1126/science.282.5386.85.

[17] L. Lampert, "High-Quality Chemical Vapor Deposition Graphene-Based Spin Transport Channels," Jan. 2000. doi: 10.15760/etd.3308.

[18] I. Žutić, J. Fabian, and S. Das Sarma, "Spintronics: Fundamentals and applications," Rev. Mod. Phys., vol. 76, no. 2, pp. 323–410, Apr. 2004, doi: 10.1103/RevModPhys.76.323.

[19] C. K. Safeer et al., "Large Multidirectional Spin-to-Charge Conversion in Low-Symmetry Semimetal MoTe2 at Room Temperature," Nano Lett., vol. 19, no. 12, pp. 8758–8766, Dec. 2019, doi: 10.1021/acs.nanolett.9b03485.

[20] C. Safranski, J. Kaiser, P. Trouilloud, P. Hashemi, G. Hu, and J. Z. Sun, "Demonstration of Nanosecond Operation in Stochastic Magnetic Tunnel Junctions," Nano Lett., vol. 21, no. 5, pp. 2040–2045, Mar. 2021, doi: 10.1021/acs.nanolett.0c04652.

[21] W. Han, R. K. Kawakami, M. Gmitra, and J. Fabian, "Graphene spintronics," Nature Nanotech, vol. 9, no. 10, pp. 794–807, Oct. 2014, doi: 10.1038/nnano.2014.214.

[22] R. J. Elliott, 'Theory of the Effect of Spin-Orbit Coupling on Magnetic Resonance in Some Semiconductors', Phys. Rev., vol. 96, no. 2, pp. 266–279, Oct. 1954, doi: 10.1103/PhysRev.96.266.

[23] Y. Yafet, "Solid State Physics, Volume 14 - 1st Edition", F. Seitz and D. Turnbull, Eds., Academic Press, 1963. isbn: 9780080864785.

[24] M. Gmitra, D. Kochan, P. Högl, and J. Fabian, "Trivial and inverted Dirac bands and the emergence of quantum spin Hall states in graphene on transition-metal dichalcogenides," Phys. Rev. B, vol. 93, no. 15, p. 155104, Apr. 2016, doi: 10.1103/PhysRevB.93.155104.

[25] J. Balakrishnan et al., "Giant spin Hall effect in graphene grown by chemical vapour deposition," Nat Commun, vol. 5, no. 1, p. 4748, Sep. 2014, doi: 10.1038/ncomms5748.

[26] M. Wojtaszek, I. J. Vera-Marun, E. Whiteway, M. Hilke, and B. J. van Wees, "Absence of hyperfine effects in ^{13}C-graphene spin-valve devices," Phys. Rev. B, vol. 89, no. 3, p. 035417, Jan. 2014, doi: 10.1103/PhysRevB.89.035417.

[27] E. J. Duplock, M. Scheffler, and P. J. D. Lindan, "Hallmark of Perfect Graphene," Phys. Rev. Lett., vol. 92, no. 22, p. 225502, Jun. 2004, doi: 10.1103/PhysRevLett.92.225502.

[28] K. M. McCreary, A. G. Swartz, W. Han, J. Fabian, and R. K. Kawakami, "Magnetic Moment Formation in Graphene Detected by Scattering of Pure Spin Currents," Phys. Rev. Lett., vol. 109, no. 18, p. 186604, Nov. 2012, doi: 10.1103/PhysRevLett.109.186604.

[29] J. Wang, F. Ma, and M. Sun, "Graphene, hexagonal boron nitride, and their heterostructures: properties and applications," RSC Adv., vol. 7, no. 27, pp. 16801–16822, Mar. 2017, doi: 10.1039/C7RA00260B.

[30] C. Lee, X. Wei, J. W. Kysar, and J. Hone, "Measurement of the Elastic Properties and Intrinsic Strength of Monolayer Graphene," Science, vol. 321, no. 5887, pp. 385–388, Jul. 2008, doi: 10.1126/science.1157996.

[31] K. I. Bolotin et al., "Ultrahigh electron mobility in suspended graphene," Solid State Communications, vol. 146, no. 9–10, pp. 351–355, Jun. 2008, doi: 10.1016/j.ssc.2008.02.024.

[32] A. K. Geim, "Graphene: Status and Prospects," Science, vol. 324, no. 5934, pp. 1530–1534, Jun. 2009, doi: 10.1126/science.1158877.

[33] A. Avsar et al., "Spin–orbit proximity effect in graphene," Nat Commun, vol. 5, no. 1, p. 4875, Sep. 2014, doi: 10.1038/ncomms5875.

[34] G. Yang, L. Li, L. W.B., and M. Ng, "Structure of graphene and its disorders: a review," Science and Technology of Advanced Materials, vol. 19, pp. 613–648, Aug. 2018, doi: 10.1080/14686996.2018.1494493.

[35] A. C. Ferrari and D. M. Basko, "Raman spectroscopy as a versatile tool for studying the properties of graphene," Nature Nanotech, vol. 8, no. 4, pp. 235–246, Apr. 2013, doi: 10.1038/nnano.2013.46.

[36] M. Xu, D. Fujita, J. Gao, and N. Hanagata, "Auger Electron Spectroscopy: A Rational Method for Determining Thickness of Graphene Films," ACS Nano, vol. 4, no. 5, pp. 2937–2945, May 2010, doi: 10.1021/nn100276w.

[37] H. Hiura, H. Miyazaki, and K. Tsukagoshi, "Determination of the Number of Graphene Layers: Discrete Distribution of the Secondary Electron Intensity Derived from Individual Graphene Layers," Appl. Phys. Express, vol. 3, no. 9, p. 095101, Aug. 2010, doi: 10.1143/APEX.3.095101.

[38] Y. Zhang and C. Pan, "Measurements of mechanical properties and number of layers of graphene from nano-indentation," Diamond and Related Materials, vol. 24, pp. 1–5, Apr. 2012, doi: 10.1016/j.diamond.2012.01.033.

[39] H. Jussila, H. Yang, N. Granqvist, and Z. Sun, "Surface plasmon resonance for characterization of large-area atomic-layer graphene film," Optica, OPTICA, vol. 3, no. 2, pp. 151–158, Feb. 2016, doi: 10.1364/OPTICA.3.000151.

[40] P. E. Gaskell, H. S. Skulason, C. Rodenchuk, and T. Szkopek, "Counting graphene layers on glass via optical reflection microscopy," Applied Physics Letters, vol. 94, no. 14, p. 143101, Apr. 2009, doi: 10.1063/1.3115026.

[41] M. S. M. de Sousa and W. Chen, "Opacity of graphene independent of light frequency and polarization due to the topological charge of the Dirac points," Phys. Rev. B, vol. 108, no. 16, p. 165201, Oct. 2023, doi: 10.1103/PhysRevB.108.165201.

[42] E. McCann, "Electronic properties of monolayer and bilayer graphene," 2011, pp. 237–275. doi: 10.1007/978-3-642-22984-8_8.

[43] N. Tombros, C. Jozsa, M. Popinciuc, H. T. Jonkman, and B. J. van Wees, "Electronic spin transport and spin precession in single graphene layers at room temperature," Nature, vol. 448, no. 7153, pp. 571–574, Aug. 2007, doi: 10.1038/nature06037.

[44] M. Drögeler et al., "Spin Lifetimes Exceeding 12 ns in Graphene Nonlocal Spin Valve Devices," Nano Lett., vol. 16, no. 6, pp. 3533–3539, Jun. 2016, doi: 10.1021/acs.nanolett.6b00497.

[45] J. Fabian, A. Matos-Abiague, C. Ertler, P. Stano, and I. Zutic, "Semiconductor spintronics," Acta Physica Slovaca 57(4&5), pp. 565–907, 2007.

[46] M. A. Hoque, L. Sjöström, D. Khokhriakov, B. Zhao, and S. P. Dash, 'Room temperature nonlocal detection of charge-spin interconversion in a topological insulator', npj 2D Mater Appl, vol. 8, no. 1, pp. 1–8, Feb. 2024, doi: 10.1038/s41699-024-00447-y.

[47] K. S. Novoselov et al., 'Two-dimensional atomic crystals', Proceedings of the National Academy of Sciences, vol. 102, no. 30, pp. 10451–10453, Jul. 2005, doi: 10.1073/pnas.0502848102.

[48] A. Avsar, H. Ochoa, F. Guinea, B. Özyilmaz, B. J. van Wees, and I. J. Vera-Marun, 'Colloquium: Spintronics in graphene and other two-dimensional materials', Rev. Mod. Phys., vol. 92, no. 2, p. 021003, Jun. 2020, doi: 10.1103/RevModPhys.92.021003.

[49] A. Avsar et al., 'Toward Wafer Scale Fabrication of Graphene Based Spin Valve Devices', Nano Lett., vol. 11, no. 6, pp. 2363–2368, Jun. 2011, doi: 10.1021/nl200714q.

[50] W. Fu, P. Makk, R. Maurand, M. Bräuninger, and C. Schönenberger, 'Large-scale fabrication of BN tunnel barriers for graphene spintronics', Journal of Applied Physics, vol. 116, no. 7, p. 074306, Aug. 2014, doi: 10.1063/1.4893578.

[51] A. L. Friedman, O. M. J. van 't Erve, C. H. Li, J. T. Robinson, and B. T. Jonker, 'Homoepitaxial tunnel barriers with functionalized graphene-on-graphene for charge and spin transport', Nat Commun, vol. 5, no. 1, p. 3161, Jan. 2014, doi: 10.1038/ncomms4161.

[52] B. Zhao et al., 'Electrically controlled spin-switch and evolution of Hanle spin precession in graphene', 2D Mater., vol. 6, no. 3, p. 035042, Jun. 2019, doi: 10.1088/2053-1583/ab1d83.

[53] M. Shiraishi et al., 'Robustness of Spin Polarization in Graphene-Based Spin Valves', Advanced Functional Materials, vol. 19, no. 23, pp. 3711–3716, 2009, doi: 10.1002/adfm.200900989.

[54] F. Liu, Y. Liu, J. Hu, D. L. Smith, and P. Paul Ruden, 'Rashba-induced spin scattering at graphene edges', Journal of Applied Physics, vol. 114, no. 9, p. 093708, Sep. 2013, doi: 10.1063/1.4820463.

[55] S. Bunaiyan, S. Datta, and K. Y. Camsari, 'Heisenberg machines with programmable spin circuits', Phys. Rev. Appl., vol. 22, no. 1, p. 014014, Jul. 2024, doi: 10.1103/PhysRevApplied.22.014014.

A
Fabrication

Fabrication done as a part for this master's thesis project is presented in this appendix. All fabrication was done in cleanroom facilities at Myfab Chalmers.

A.1 Fabrication process for the spintronic devices on chip Gr-1

Chip Gr-1 containing nine spintronic devices of chemical vapor deposition (CVD) graphene with ferromagnetic (FM) Co/TiO_2 and nonmagnetic (NM) Au/Ti contacts was fabricated as a part of this master's thesis project. The fabrication recipe is described here.

A.1.1 Mask design

Software AutoCAD was used to design the mask for electron beam lithography (EBL). Each device has graphene patterns of width between 1.5 - 3 µm, NM contacts (purple) of width 1.6 - 3.2 µm and FM contacts (orange) of width 50 - 550 nm. This gave each FM contact its own individual width and therefore an individual coercivity (see Section 2.2.1). An example of a mask design can be seen in Figure A.1 (a).

A.1.2 Chip preparation

A 7 x 7 mm chip was cut out of a 4" Si/SiO_2 wafer with CVD graphene prepared by Grolltex Inc and protective resist on-top. The protective resist was removed by cleaning the chip with acetone at 80 °C for 5 minutes, then in acetone at room temperature (RT) for 2 minutes followed by isopropyl alcohol (IPA) at RT for 2 minutes. The chip was then carefully dried by N_2 blow drying.

A.1.3 Electron beam lithography for graphene patterns

After cleaning, the chip had to be prepared for EBL. This was done by spin coating two layers of resist onto the chip. The first layer was done by spinning MMA8.5MAA EL8 for 60 seconds with a rotation speed of 6000 rpm and an acceleration of 3000 rpm/s. This was followed with soft baking at 130 °C for 10 minutes. The second layer was done by spinning ARP 6200 13 1:2 for 60 seconds with a rotation speed of 6000 rpm and an acceleration of 3000 rpm/s. This was followed with soft baking

at 130 °C for 10 minutes.

Next step was to expose the resist using EBL according to graphene patterns (see Section A.1.1), which was done with an electron beam current of 2 nA and a dose of 240 µm/cm^2. The resist was then developed in n-amyl acetone for 1 minute and 15 seconds followed by MIBK:IPA 1:1 for 45 seconds.

The chip was then etched using oxygen plasma with a power of 25 W for 30 seconds to remove all non-protected and unwanted graphene. All remaining resist was then removing by cleaning in acetone at 80 °C for 5 minutes and in acetone at RT for 2 minutes min followed by IPA at RT for 2 minutes. Chip was then carefully dried with N_2 blow dry.

A.1.4 Electron beam lithography, physical evaporation deposition and lift-off for nonmagnetic contacts

Two resist layers were spin coated and soft baked using the same process as described in Section A.1.3 and then exposed using EBL according to the NM contacts pattern (see Section A.1.1). The exposure was done in two steps. First a smaller current of 2 nA and a smaller dose of 240 µm/cm^2 was used to expose the smaller details around the device to minimise proximity effects, then a larger current of 35 nA and a larger dose of 350 µm/cm^2 was used to expose parts of contacts far away from device to speed up exposure time. The resist was then developed using the same process as described in Section A.1.3.

Electron-beam physical vapor deposition (EB-PVD) in a high vacuum chamber ($1 - 2 \cdot 10^{-7}$ Torr) were used to deposit 15 nm of Ti followed by 80 nm of Au. The Ti layer is used to aid Au adhere to the SiO_2 layer.

Since deposition deposits metal everywhere on the chip, it was needed to remove unwanted metal to create the desired contacts. This was done by performing lift-off, where the edges of the chip were scratched carefully with a scalpel to expose the resist below for solvents. The chip was then put in acetone at 80 °C until unwanted metals were lifted off. The chip was then cleaned in acetone at 80 °C for 5 minutes, then in acetone at RT for 2 minutes followed by IPA at RT for 2 minutes.

A.1.5 Electron beam lithography, physical evaporation deposition and lift-off for magnetic contacts

Three resist layers were spin coated and soft baked. The first layer was done by spinning MMA8.5 MAA EL6 for 60 seconds with a rotation speed of 3000 rpm and an acceleration of 1000 rpm/s followed by soft baking at 130 °C for 3 minutes. AR-P 6200.13 1:2 was then spin coated on-top for 60 seconds with a rotation speed of 6000 rpm and an acceleration of 1000 rpm/s followed by soft baking at 130 °C for 3 minutes. Next layer was done by spinning 950 PMMA A3 for 60 seconds with a rotation speed of 6000 rpm and an acceleration of 1000 rpm/s, and was soft baked

at 130 °C for 3 minutes. A conducting layer of Espacer 300Z to avoid charge-up was added on top of this by spinning for 60 seconds with a rotation speed of 2800 rpm and an acceleration of 1000 rpm/s. Unlike the previous layers, this last conducting layer does not need to be soft baked.

The resist was then exposed using EBL according to the FM contacts pattern mentioned in Section A.1.1. The exposure was done in two steps, one with a low current (2 nA) and a low dose (240 µm/cm^2) and the other with a larger current (100 nA) and a larger dose (350 µm/cm^2). The reason for this is the same as for NM contacts (see Section A.1.4). The chip was first cleaned in H_2O for 30 seconds to remove the conducting layer, then developed in H_2O:IPA 7:93 for 60 seconds, n-amyl acetate for 60 seconds and MIBK:IPA 1:3 for 60 seconds, and then carefully blow dried with N_2.

2 Å of Ti were deposited using EB-PVD in a high vacuum chamber ($8{\cdot}10^{-7}$ Torr) and oxidised by pumping in oxygen into the chamber until chamber reached a pressure of 10 Torr. It was then left to oxidise for 10 minutes before pumped down again to deposit 60 nm of Co in high vacuum ($4.2 - 4.5 \cdot 10^{-7}$ Torr) and 2 nm of Al in high vacuum ($4.1 \cdot 10^{-7}$ Torr). The desired design was then achieved after performing lift-off as described in Section A.1.4. Example of completed device can be seen in Figure A.1 (b).

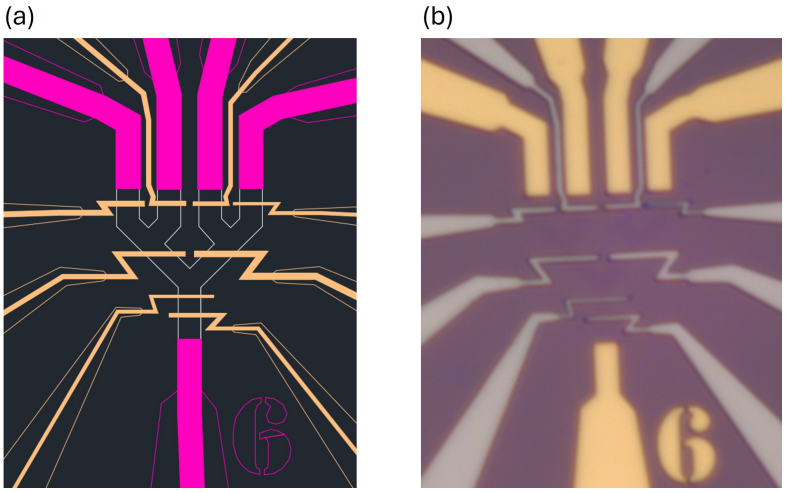

Figure A.1: Device 6 on chip Gr-1. (a) Mask design for graphene (white), nonmagnetic gold contacts (purple) and magnetic cobalt contacts (orange) made in AutoCAD. (b) Microscopic image of final device, where graphene can be faintly spotted with a darker texture compared to the SiO_2 background, nonmagnetic gold contacts with a yellow colour and magnetic cobalt contacts with a grey colour.

A.2 Fabrication process for the spintronic devices on chip Gr-2

Chip Gr-2 consists of 15 spintronic devices of CVD graphene with FM Co/TiO_2 contacts and was fabricated as a part of this master's thesis project. The fabrication process is described here.

A.2.1 Mask design

A mask for graphene pattern and magnetic contacts to be used in EBL was designed using software AutoCAD. The graphene patterns width ranged from 100 nm to 3 µm and the magnetic contacts width ranged from 50 nm to 600 nm (1.5 µm for reference contacts). An example of a mask design can be seen in Figure A.2.

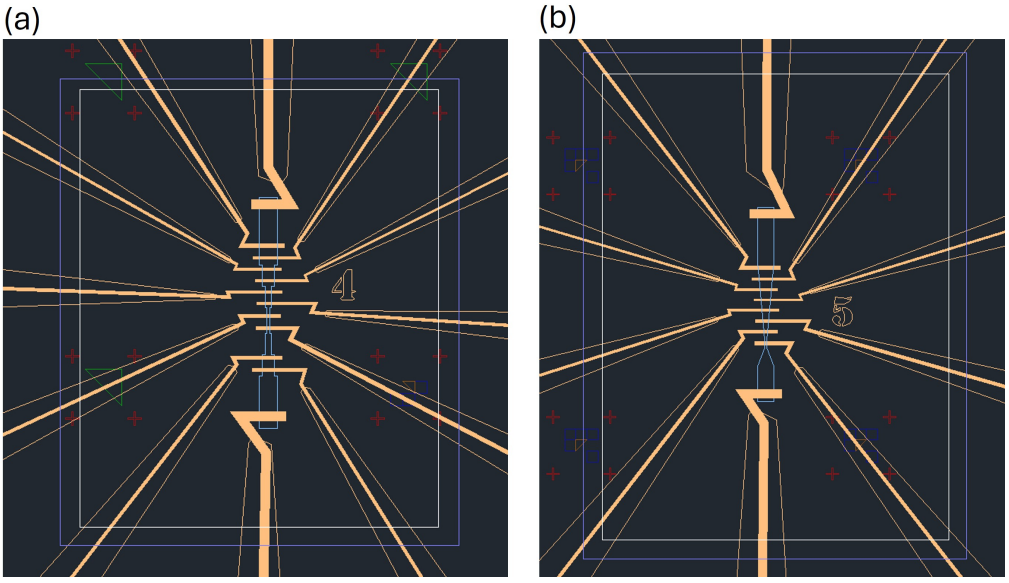

Figure A.2: Mask designs for device 4 (a) and device 5 (b) on chip Gr-2 using software AutoCAD. Graphene pattern is highlighted in light blue and magnetic cobalt contacts in orange. The violet (white) square around the device denotes where low current exposure ends (high current exposure begins) for graphene EBL exposure.

A.2.2 Chip preparation

A 7 x 7 mm chip was cut out from a Si/SiO_2 wafer with CVD graphene and a protective resist on-top. The protective resist was removed by cleaning the chip by first putting the chip in acetone at 80 °C for 5 minutes followed by 2 minutes in RT acetone and 2 minutes in RT IPA and carefully dried by N_2 blow drying.

A.2.3 Electron beam lithography for graphene patterns

Three layers of resist were spin coated and soft baked on-top of the graphene. Spin coating MMA8.5 MAA EL6 for 60 seconds with a rotation speed of 3000 rpm and an acceleration of 1000 rpm/s and soft baking at 130 °C for 3 minutes was done to make the first layer. For the second layer, AR-P 6200.13 1:2 was spin coated for 60 seconds with a rotation speed of 6000 rpm and an acceleration of 1000 rpm/s followed by soft baking at 130 °C. 950 PMMA A3 was spin coated for the last resist layer for 60 seconds with a rotation speed of 6000 rpm and an acceleration of 1000 rpm/s and soft baking at 130 °C for 3 minutes. A conducting layer was added on top of this by spinning Espacer 300Z for 60 seconds with a rotation speed of 2800 rpm and an acceleration of 1000 rpm/s and no soft baking.

The resist was then exposed using EBL according to the graphene patterns mask design (see Section A.2.1), which was done with 2 steps, one low current and one high current. First, a low current of 2 nA were used to expose around the devices, with varying doses calculated to minimise proximity effect. A higher current of 100 nA and a dose of 350 µm/cm^2 were used to expose parts further away from the device where the proximity effect from this exposure would not affect the resist close to devices. After exposure, the chip was first cleaned in H_2O for 30 seconds to remove the conducting layer, then developed in H_2O:IPA 7:93 for 60 seconds, n-amyl acetate for 60 seconds and MIBK:IPA 1:3 for 60 seconds, and then carefully blow dried with N_2.

With unwanted graphene now exposed after development, this graphene was removed by oxygen plasma etching, which was done with a power of 25 W for 30 seconds. The rest of the resist was then removed by cleaning the chip in acetone at 80 °C for 5 minutes followed by acetone at RT for 2 minutes and IPA at RT for 2 minutes. Chip was then carefully dried with N_2 blow dry. Example of etched graphene can be seen in Figure A.3.

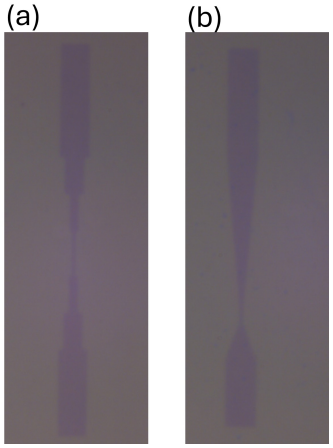

Figure A.3: Microscopy images of device 4 (a) and device 5 (b) after etching graphene.

A.2.4 Electron beam lithography, physical evaporation deposition and lift-off for magnetic contacts

Four layers of resist were spin coated, soft baked, exposed using EBL according to the magnetic contacts mask (see Section A.2.1) and developed with the same processes as described in Section A.2.3.

The TiO_2 TB was created by first depositing 2 Å of Ti at high vacuum ($8 \cdot 10^{-7}$ Torr) by EB-PVD, and then decreasing pressure in the chamber to 10 Torr and letting the Ti oxidise for 10 minutes. The chamber was then pumped back down to high vacuum ($4.1 - 4.5 \cdot 10^{-7}$ Torr) to deposit 60 nm of Co and 2 nm of Al.

Lift-off was performed to remove unwanted deposited metal. First, the edges of the chip were scratched carefully with a scalpel to create a path for chemicals to reach the resist below. The chip was then set in acetone at 80 °C until all unwanted metals were removed from chip. The chip was then cleaned according to the same cleaning process described in Section A.2.2. Example of completed devices is shown in Figure A.4.

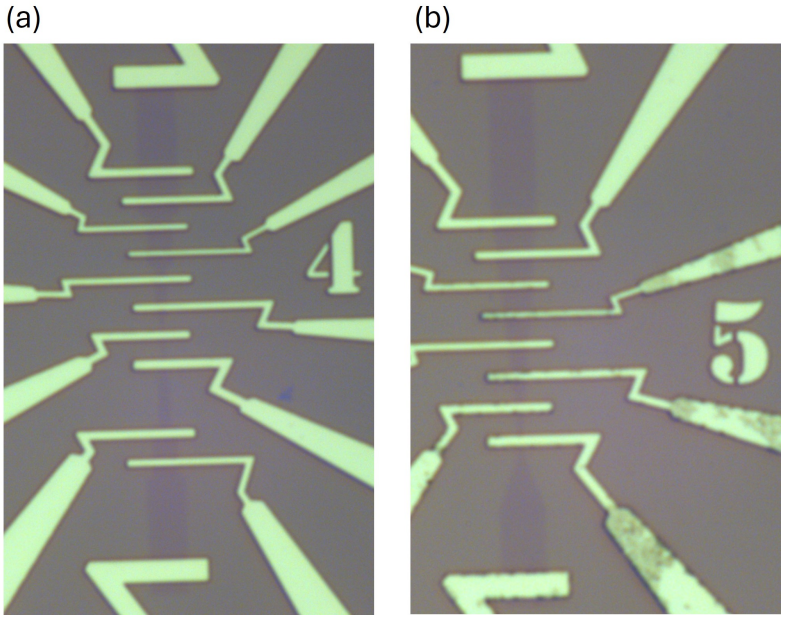

Figure A.4: Microscopy images of device 4 (a) and device 5 (b). Graphene can be seen with a darker texture compared to the SiO_2 background and magnetic cobalt contacts with a green colour.

DEPARTMENT OF MICROTECHNOLOGY AND NANOSCIENCE
CHALMERS UNIVERSITY OF TECHNOLOGY
Gothenburg, Sweden
www.chalmers.se

CHALMERS
UNIVERSITY OF TECHNOLOGY